Design of the ECCE Detector for the Electron Ion Collider

J. K. Adkins[33], Y. Akiba[51,55], A. Albataineh[70], M. Amaryan[44], I. C. Arsene[74], C. Ayerbe Gayoso[35], J. Bae[60], X. Bai[80], M.D. Baker[5,27], M. Bashkanov[89], R. Bellwied[68], F. Benmokhtar[15], V. Berdnikov[13], J. C. Bernauer[53,54,55], F. Bock[46], W. Boeglin[16], M. Borysova[84], E. Brash[11], P. Brindza[27], W. J. Briscoe[20], M. Brooks[30], S. Bueltmann[44], M. H. S. Bukhari[26], A. Bylinkin[70], R. Capobianco[66], W.-C. Chang[2], Y. Cheon[58], K. Chen[8], K.-F. Chen[43], K.-Y. Cheng[37], M. Chiu[5], T. Chujo[77], Z. Citron[4], E. Cline[53,54], E. Cohen[41], E. Conroy[47], T. Cormier[46,*], Y. Corrales Morales[30], C. Cotton[80], J. Crafts[13], C. Crawford[71], S. Creekmore[46], C.Cuevas[27], J. Cunningham[46], G. David[5], C. T. Dean[30], M. Demarteau[46], S. Diehl[66], N. Doshita[86], R. Dupré[22], J. M. Durham[30], R. Dzhygadlo[19], R. Ehlers[46], L. El Fassi[35], A. Emmert[80], R. Ent[27], C. Fanelli[34,85,27], R. Fatemi[71], S. Fegan[89], M. Finger[9], M. Finger Jr.[9], J. Frantz[45], M. Friedman[21], I. Friscic[34,27], D. Gangadharan[68], S. Gardner[18], K. Gates[18], F. Geurts[50], R. Gilman[52], D. Glazier[18], E. Glimos[46,79], Y. Goto[51,55], N. Grau[3], S. V. Greene[81], A. Q. Guo[24], L. Guo[16], C. Gwenlan[47], S. K. Ha[87], J. Haggerty[5], T. Hayward[66], X. He[17], O. Hen[34], D. W. Higinbotham[27], M. Hoballah[22], T. Horn[13], A. Hoghmrtsyan[1], P.-h. J. Hsu[42], J. Huang[5], G. Huber[75], A. Hutson[68], K. Y. Hwang[88], C. E. Hyde[44], M. Inaba[64], T. Iwata[86], H.S. Jo[29], K. Joo[66], N. Kalantarians[82], G. Kalicy[13], K. Kawade[59], S. J. D. Kay[75], A. Kim[66], B. Kim[60], C. Kim[49], M. Kim[51], Y. Kim[49], Y. Kim[58], E. Kistenev[5], V. Klimenko[66], S. H. Ko[57], I. Korover[34], W. Korsch[71], G. Krintiras[70], S. Kuhn[44], C.-M. Kuo[37], T. Kutz[34], J. Lajoie[25], D. Lawrence[27], S. Lebedev[25], H. Lee[60], J. S. H. Lee[76], S. W. Lee[29], Y.-J. Lee[34], W. Li[50], W.B. Li[53,54,85], X. Li[62], X. Li[10], X. Li[30], X. Li[34], Y. T. Liang[24], S. Lim[49], C.-H. Lin[2], D. X. Lin[24], K. Liu[30], M. X. Liu[30], K. Livingston[18], N. Liyanage[80], W.J. Llope[83], C. Loizides[46], E. Long[73], R.-S. Lu[43], Z. Lu[10], W. Lynch[89], S. Mantry[67], D. Marchand[22], M. Marcisovsky[14], C. Markert[78], P. Markowitz[16], H. Marukyan[1], P. McGaughey[30], M. Mihovilovic[72], R. G. Milner[34], A. Milov[84], Y. Miyachi[86], A. Mkrtchyan[1], H. Mkrtchyan[1], P. Monaghan[11], R. Montgomery[18], D. Morrison[5], A. Movsisyan[1], C. Munoz Camacho[22], M. Murray[70], K. Nagai[30], J. Nagle[65], I. Nakagawa[51], C. Nattrass[79], D. Nguyen[27], S. Niccolai[22], R. Nouicer[5], G. Nukazuka[51], M. Nycz[80], V. A. Okorokov[40], S. Orešić[75], J.D. Osborn[46], C. O'Shaughnessy[30], S. Paganis[43], Z. Papandreou[75], S. F. Pate[39], M. Patel[25], C. Paus[34], G. Penman[18], M. G. Perdekamp[69], D. V. Perepelitsa[65], H. Periera da Costa[30], K. Peters[19], W. Phelps[11], E. Piasetzky[61], C. Pinkenburg[5], I. Prochazka[9], T. Protzman[31], M. L. Purschke[5], J. Putschke[83], J. R. Pybus[34], R. Rajput-Ghoshal[27], J. Rasson[46], B. Raue[16], K.F. Read[46,79], K. Røed[74], R. Reed[31], J. Reinhold[16], E. L. Renner[30], J. Richards[66], C. Riedl[69], T. Rinn[5], J. Roche[45], G. M. Roland[34], G. Ron[21], M. Rosati[25], C. Royon[70], J. Ryu[49], S. Salur[52], N. Santiesteban[34], R. Santos[66], M. Sarsour[17], J. Schambach[46], A. Schmidt[20], N. Schmidt[46], C. Schwarz[19], J. Schwiening[19], R. Seidl[51,55], A. Sickles[69], P. Simmerling[66], S. Sirca[72], D. Sharma[17], Z. Shi[30], T.-A. Shibata[38], C.-W. Shih[37], S. Shimizu[51], U. Shrestha[66], K. Slifer[73], K. Smith[30], D. Sokhan[18,23], R. Soltz[32], W. Sondheim[30], J. Song[10], J. Song[49], I. I. Strakovsky[20], P. Steinberg[5], P. Stepanov[13], J. Stevens[85], J. Strube[48], P. Sun[10], X. Sun[8], K. Suresh[75], V. Tadevosyan[1], W.-C. Tang[37], S. Tapia Araya[25], S. Tarafdar[81], L. Teodorescu[6], D. Thomas[78], A. Timmins[68], L. Tomasek[14], N. Trotta[66], R. Trotta[13], T. S. Tveter[74], E. Umaka[25], A. Usman[75], H. W. van Hecke[30], C. Van Hulse[22], J. Velkovska[81], E. Voutier[22], P.K. Wang[22], Q. Wang[70], Y. Wang[8], Y. Wang[63], D. P. Watts[89], N. Wickramaarachchi[13], L. Weinstein[44], M. Williams[34], C.-P. Wong[30], L. Wood[48], M. H. Wood[7], C. Woody[5], B. Wyslouch[34], Z. Xiao[63], Y. Yamazaki[28], Y. Yang[36], Z. Ye[63], H. D. Yoo[88], M. Yurov[30], N. Zachariou[89], W.A. Zajc[12], W. Zha[62], J.-L. Zhang[56], J.-X. Zhang[80], Y. Zhang[63], Y.-X. Zhao[24], X. Zheng[80], P. Zhuang[63]

[1] *A. Alikhanyan National Laboratory, Yerevan, Armenia*
[2] *Institute of Physics, Academia Sinica, Taipei, Taiwan*
[3] *Augustana University, Sioux Falls, SD, USA*
[4] *Ben-Gurion University of the Negev Beer-Sheva, Israel*
[5] *Brookhaven National Laboratory, Upton, NY, USA*
[6] *Brunel University London, Uxbridge, UK*
[7] *Canisius College, Buffalo, NY, USA*
[8] *Central China Normal University, Wuhan, China*
[9] *Charles University, Prague, Czech Republic*
[10] *China Institute of Atomic Energy, Fangshan, Beijing, China*
[11] *Christopher Newport University, Newport News, VA, USA*
[12] *Columbia University, New York, NY, USA*
[13] *Catholic University of America, Washington DC, USA*
[14] *Czech Technical University, Prague, Czech Republic*
[15] *Duquesne University, Pittsburgh, PA, USA*
[16] *Florida International University, Miami, FL, USA*
[17] *Georgia State University, Atlanta, GA, USA*
[18] *University of Glasgow, Glasgow, UK*
[19] *GSI Helmholtzzentrum fuer Schwerionenforschung GmbH, Darmstadt, Germany*
[20] *The George Washington University, Washington, DC, USA*
[21] *Hebrew University, Jerusalem, Isreal*

[*] Deceased

[22]Universite Paris-Saclay, CNRS/IN2P3, IJCLab, Orsay, France
[23]IRFU, CEA, Universite Paris-Saclay, Gif-sur-Yvette France
[24]Chinese Academy of Sciences, Lanzhou, China
[25]Iowa State University, Iowa City, IA, USA
[26]Jazan University, Jazan, Sadui Arabia
[27]Thomas Jefferson National Accelerator Facility, Newport News, VA, USA
[28]Kobe University, Kobe, Japan
[29]Kyungpook National University, Daegu, Republic of Korea
[30]Los Alamos National Laboratory, Los Alamos, NM, USA
[31]Lehigh University, Bethlehem, PA, USA
[32]Lawrence Livermore National Laboratory, Livermore, CA, USA
[33]Morehead State University, Morehead, KY,
[34]Massachusetts Institute of Technology, Cambridge, MA, USA
[35]Mississippi State University, Mississippi State, MS, USA
[36]National Cheng Kung University, Tainan, Taiwan
[37]National Central University, Chungli, Taiwan
[38]Nihon University, Tokyo, Japan
[39]New Mexico State University, Las Cruces, NM, USA
[40]National Research Nuclear University MEPhI, Moscow, Russian Federation
[41]Nuclear Research Center - Negev, Beer-Sheva, Isreal
[42]National Tsing Hua University, Hsinchu, Taiwan
[43]National Taiwan University, Taipei, Taiwan
[44]Old Dominion University, Norfolk, VA, USA
[45]Ohio University, Athens, OH, USA
[46]Oak Ridge National Laboratory, Oak Ridge, TN, USA
[47]University of Oxford, Oxford, UK
[48]Pacific Northwest National Laboratory, Richland, WA, USA
[49]Pusan National University, Busan, Republic of Korea
[50]Rice University, Houston, TX, USA
[51]RIKEN Nishina Center, Wako, Saitama, Japan
[52]The State University of New Jersey, Piscataway, NJ, USA
[53]Center for Frontiers in Nuclear Science, Stony Brook, NY, USA
[54]Stony Brook University, Stony Brook, NY, USA
[55]RIKEN BNL Research Center, Upton, NY, USA
[56]Shandong University Qingdao, Shandong, China
[57]Seoul National University, Seoul, Republic of Korea
[58]Sejong University, Seoul, Republic of Korea
[59]Shinshu University, Matsumoto, Nagano, Japan
[60]Sungkyunkwan University, Suwon, Republic of Korea
[61]Tel Aviv University, Tel Aviv, Israel
[62]University of Science and Technology of China, Hefei, China
[63]Tsinghua University, Beijing, China
[64]Tsukuba University of Technology, Tsukuba, Ibaraki, Japan
[65]University of Colorado Boulder, Boulder, CO, USA
[66]University of Connecticut, Storrs, CT, USA
[67]University of North Georgia, Dahlonega GA, USA
[68]University of Houston, Houston, TX, USA
[69]University of Illinois, Urbana, IL, USA
[70]Unviersity of Kansas, Lawrence, KS, USA
[71]University of Kentucky, Lexington, KY, USA
[72]University of Ljubljana, Ljubljana, Slovenia, Ljubljana, Slovenia
[73]University of New Hampshire, Durham, NH, USA
[74]University of Oslo, Oslo, Norway
[75] University of Regina, Regina, SK, Canada
[76]University of Seoul, Seoul, Republic of Korea
[77]University of Tsukuba, Tsukuba, Japan
[78]University of Texas, Austin, Texas, USA
[79]University of Tennessee, Knoxville, TN, USA
[80]University of Virginia, Charlottesville, VA, USA
[81]Vanderbilt University, Nashville, TN, USA
[82]Virginia Union University, Richmond, VA, USA
[83]Wayne State University, Detroit, MI, USA
[84]Weizmann Institute of Science, Rehovot, Israel
[85]The College of William and Mary, Williamsburg, VA, USA
[86]Yamagata University, Yamagata, Japan
[87]Yarmouk University, Irbid, Jordan
[88]Yonsei University, Seoul, Republic of Korea
[89]University of York, York, UK

Abstract

The EIC Comprehensive Chromodynamics Experiment (ECCE) detector has been designed to address the full scope of the proposed Electron Ion Collider (EIC) physics program as presented by the National Academy of Science and provide a deeper understanding of the quark-gluon structure of matter. To accomplish this, the ECCE detector offers nearly acceptance and energy coverage along with excellent tracking and particle identification. The ECCE detector was designed to be built within the budget envelope set out by the EIC project while simultaneously managing cost and schedule risks. This detector concept has been selected to be the basis for the EIC project detector.

Keywords: ECCE, Electron Ion Collider, Tracking, Calorimetry, PID

Contents

1. Introduction

The physics program at the Electron-Ion Collider (EIC) – planned for construction at Brookhaven National Laboratory (BNL), in close partnership with the Thomas Jefferson National Accelerator Facility (TJNAF) – will be the culmination of decades of research into the quark and gluon substructure of hadrons and nuclei. It will provide scientific opportunities well into the next three decades. The EIC will address a broad set of scientific questions whose impact and context were assessed in a major 2018 report by the National Academies of Science (NAS) [1]:

- While the longitudinal momenta of quarks and gluons in nucleons and nuclei have been measured with great precision at previous facilities – most notably CEBAF at JLab and the HERA collider at DESY – the full three-dimensional momentum and spatial structure of nucleons and nuclei has yet to be fully elucidated, particularly including spin, which requires the separation of the intrinsic spin of the constituent particles from their orbital motion.
- These studies will also provide insight into how the mutual interactions of quarks and gluons generate the mass of nucleons and other hadrons. The nucleon mass is one of the single most important scales in all of physics, as it is the basis for nuclear masses, and thus the mass of essentially all of visible matter in the universe.
- The density of quarks and gluons which carry the smallest x, the fraction of the nuclear momentum (or that of its constituent nucleons), can grow so large that their mutual interactions enter a non-linear regime in which elegant, universal features emerge in what may be a new, distinct state of matter characterized by a "saturation momentum scale". Probing this state requires high energy beams and large nuclear size (A), and will answer longstanding questions raised by the heavy ion programs at RHIC and the LHC.

To carry out this ambitious physics program, the EIC requires a comprehensive experimental program carefully designed to extract physics from the scattering of electrons off of hadrons and nuclei. The ideal EIC detector must measure nearly every particle emerging from the interaction point, including its direction, its momentum, as well as its hadron species. Each of these aspects of the EIC physics program, and how a single comprehensive detector system could address them, was studied by the EIC scientific community and led to the community-authored "Yellow Report" [2]. The report also identified a set of detector performance requirements that flowed from the physics requirements of the EIC science program articulated in the NAS report:

- The outgoing electron must be distinguished from other produced particles in the event, with a pion rejection of 10^3 — 10^4 even at large angles, in order to characterize the kinematic properties of the initial scattering process. These include the momentum fraction of the struck target constituent (x) and the squared momentum transfer (Q^2).
- A large-acceptance magnetic spectrometer is needed to measure the scattered electron momentum, as well as the

momenta of the other charged hadrons and leptons. The magnet dimensions and field strength should be matched to the scientific program and the medium-energy scale of the EIC. This requires a nearly 4π angular aperture, and the ability to make precise measurements of the momentum down to low-transverse momentum, p_t, to measure its point of origin, and to distinguish prompt particles from charm and bottom hadron decays.

- A high-purity hadron particle identification (PID) system, able to provide continuous (e/π), (K/π), and (K/p) discrimination out to the highest momentum (60 GeV), is important for identifying particles containing different light quark flavors with semi-inclusive DIS.

- A hermetic electromagnetic calorimeter system, with matching hadronic sections, is required to measure neutral particles (particularly photons and neutrons) and, in tandem with the spectrometer, to reconstruct hadronic jets. These jets carry kinematic information about the struck quark or gluon, as well as its radiative properties via its substructure.

- Far-forward detector systems, in the direction of the incoming hadron or nucleus, are needed in order to perform measurements of deeply-virtual Compton scattering and diffractive processes, e.g. by measuring the small deflections of the incoming proton and suppressing incoherent interactions with nuclei.

- Far-backward detectors, in the direction of the incoming electron, are needed to reach the very lowest values of Q^2. Also these detectors need to measure luminosity for both absolute cross-section measurements and precision spin-dependent asymmetries.

As a response to the joint BNL/JLab call for detector proposals, this document presents the EIC Comprehensive Chromodynamics Experiment (ECCE), which has been designed, simulated and extensively studied by the 96 institutes in the newly-formed ECCE proto-collaboration. The ECCE detector has been designed to address the full scope of the EIC physics program as presented in the EIC white paper [3] and the NAS report [1]. The specific requirements of each of the ECCE detector systems flows, in turn, from the more general detector requirements described in the Yellow Report [2]. Through judicious reuse of existing equipment, ECCE meets the Yellow Report requirements, and can be built within the EIC project budget.

The ECCE concept reuses the BaBar superconducting solenoid as well as the sPHENIX barrel flux return and hadronic calorimeter. These two pieces of equipment are currently being installed in RHIC Interaction Region 8 (IR8) as part of the sPHENIX detector [4]. Engineering studies have confirmed that these two components can be relocated to IR6, the IR where the EIC project currently plans to site the on-project detector. Additional details concerning ECCE subsystems, performance, and selected physics objectives are provided in separate articles within this same collection.[5, 6, 7, 8, 9, 10, 11, 12]

2. ECCE detector overview

The ECCE detector consists of three major components: the central detector, the far-forward system, and the far-backward region. The ECCE central detector has a cylindrical geometry based on the BaBar/sPHENIX superconducting solenoid, and has three primary subdivisions: the barrel, the forward endcap, and the backward endcap (Fig. 2). Henceforth "forward" is defined as the hadron/nuclear beam direction and backwards the electron beam direction. We will use electron or backward, and hadron or forward, interchangeably when describing the endcaps.

Table 1 lists the physics requirements in the ECCE central detector, the technical challenges associated with its realization, and the ECCE solutions that achieve the stated goals. Comments about future upgrade paths are also provided.

Table 2 presents similar information for the far-forward and far-backwards regions.

Figure 2 shows the ECCE central detector and lists its key components and the technology selected for each sub-system. Here, we provide general technical details on these detector technologies and their implementation:

Magnet ECCE intends to reuse the BaBar superconducting solenoid that is currently installed in the sPHENIX experiment and will be available after its conclusion. Its reuse for the EIC was the subject of an engineering study and risk analysis in 2020 [13] whose main conclusion was that the "magnet should be suitable for prolonged use as part of the detector system for the EIC project." Additional performance assessment will be conducted during an sPHENIX long-duration high field test (at 1.4 T) planned in 2022. This test, followed by the first full duration run of sPHENIX in early 2023, will validate the feasibility of its reuse in ECCE. Preparing the solenoid for reuse will involve proactive maintenance and several minor modifications. We also plan to carry through a replacement magnet engineering and design assessment as risk mitigation, as described in Section 11.

Central barrel The ECCE central barrel region comprises six subsystems:

Silicon Tracker The silicon barrel detector consists of five layers: three vertex layers close to the beam pipe and two middle layers providing the central track sagitta measurements. All layers use the ITS-3 sensors with pixel pitch at 10 μm with an average material budget of 5% of a radiation length, X_0, per layer.

μRwell Tracker The Si tracker is supplemented by two μRwell layers, cost effective micro-pattern gas detectors, between the Si sagitta layer and the hpDIRC, and a single outer barrel μRWell layer between the DIRC and BECAL.

AC-LGAD TOF A time of flight layer is placed just before the hpDIRC to provide a precise TOF measurement as well as an additional tracking point. See electron endcap discussion for details.

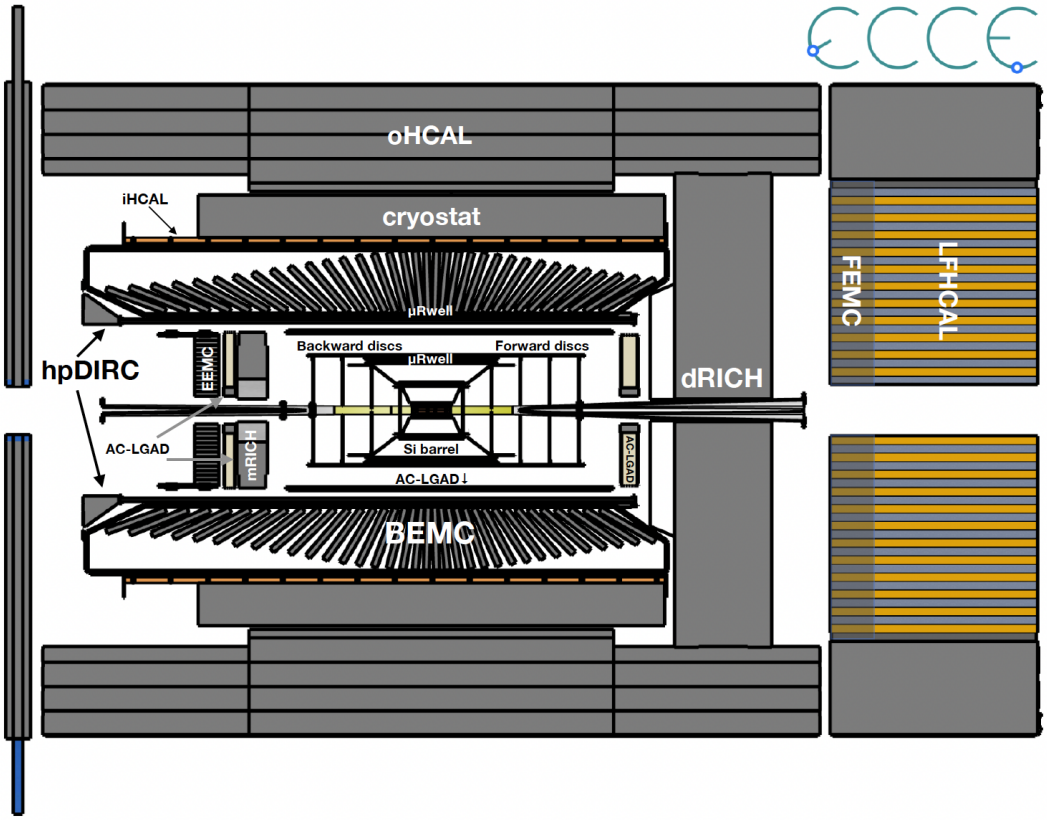

Figure 1: Side view of the full ECCE detector system, oriented with the hadron beam arriving from the left and the electron beam arriving from the right.

hpDIRC The high-performance DIRC provides particle identification with three standard deviations separation for π/K up to 6 GeV/c, e/π up to 1.2 GeV/c, and K/p up to 12 GeV/c.

BECAL The barrel ECAL (BECAL) is a homogeneous projective electromagnetic calorimeter built out of 8960 clear scintillating glass (SciGlass) towers, arranged in 70 rings in the η direction, with 128 towers per ring along ϕ. The SciGlass towers have a front face of 4 cm×4 cm and are 55 cm deep including ~10cm readout, providing 16 radiation lengths and better than $4\%/\sqrt{(E)}$ + (1–2)% energy resolution. This resolution surpasses the EIC YR requirement to complement the tracking system and ease electron identification and π/e rejection, with an eye to the future high-luminosity EIC science needs. The towers are slightly tapered to be nearly projective to the interaction point.

IHCAL/OHCAL The ECCE outer barrel hadronic calorimeter (oHCAL) is integrated into the barrel flux return for the ECCE solenoid magnet and has been built and will be optimized by the sPHENIX experiment. It consists of 32 sectors of 1020 magnet steel, with an inner and outer radius of 1.9 m and 2.6 m respectively. Each sector is 6.3 m long and weighs 14 tons. The barrel inner HCAL (iHCAL) is a hadronic calorimeter that is integrated into the BECAL support frame. Its design consists of 32 sectors of stainless steel, with an inner radius of 135 cm and an outer radius of 138.5 cm.

Electron endcap The ECCE electron endcap region comprises four subsystems:

Tracker The silicon electron endcap detector consists of four disks which provide precise measurements of charged tracks (especially electron tracks) in the backward pseudorapidity region. The technology for the silicon disks is the ITS-3 silicon sensor with pixel pitch at 10 μm. The detector mechanical structure design will be informed by the EIC eRD111 studies. In addition, the AC-LGAD TOF detectors described below will provide an additional high-precision tracking point after the disks at a large distance from the interaction point.

mRICH The design goal of the modular RICH (mRICH) is to achieve 3σ K/pi separation in the momentum range from 2 to 10 GeV/c. Excellent e/pi separation for momenta below 2 GeV/c is expected. In addition, the RICH detectors contribute to e/π identification. When combined with an EM calorimeter, the mRICH and hpDIRC will provide excellent suppression of the low-momentum charged-pion backgrounds, which limits the ability to measure the scattered electron in kinematics where it loses most of its

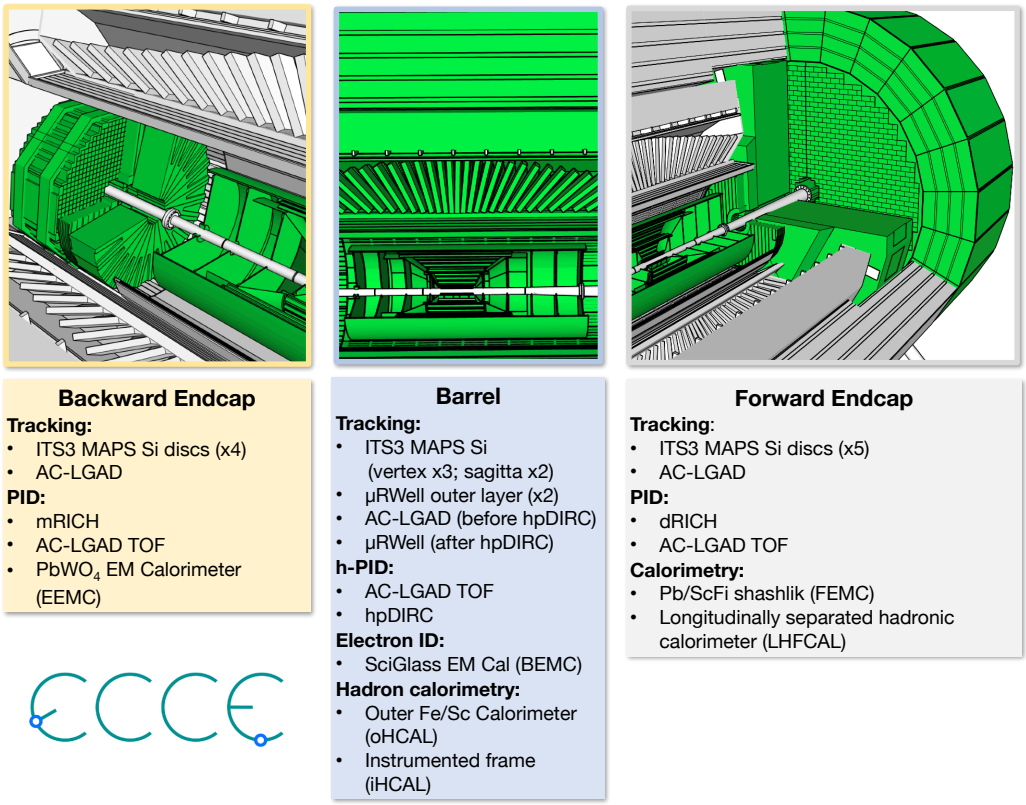

Figure 2: Principal components of the ECCE central detector: backward/electron endcap (left), barrel (center), and forward/hadron endcap (right).

energy.

AC-LGAD TOF A time of flight measurement using AC-LGAD technology will be used for PID in the momentum range below the Cherenkov detectors thresholds. These detectors also provide a high-precision tracking point.

EEMC The Electron Endcap EM Calorimeter (EEMC) is a high-resolution electromagnetic calorimeter that is capable of providing precision scattered electron and final-state photon detection in the region $-3.7 < \eta < -1.5$. The detector is comprised of 2 cm x 2 cm x 20 cm $PbWO_4$ crystals which provide 20 radiation lengths. The overall design concept is the same as in the EIC YR.

Fe flux return As an active electron endcap hadron calorimeter provides no substantial benefits to the scientific program, the iron flux return will be passive. We note that adequate space remains available for a possible upgrade path towards high-luminosity running allowing the measurement of the jet distribution in the low-x, high-Q^2 region.

Hadron endcap The ECCE hadron endcap region comprises five subsystems:

Tracker The silicon hadron endcap detector consists of five disks, which provide precisely measured space points for charged particle tracking in the forward pseudorapidity region. This detector will improve the determination of the decay vertex of weakly decaying particles and measure the majority of the charged particles in asymmetric $e + p$ and $e + A$ collisions. The technology for the silicon disks is ITS-3 silicon sensor with pixel pitch of 10 µm. The detector mechanical structure design will be informed by the EIC eRD111 studies. An AC-LGAD TOF detector placed in front of the dRICH will provide an additional high-precision tracking point.

AC-LGAD TOF See electron endcap for details.

dRICH The dual-radiator Ring Imaging Cherenkov (dRICH) detector is designed to provide continuous hadron identification in the (outgoing) ion-side with 3σ or more for π/K from ~0.7 GeV/c to ~50 GeV/c, and for e/π from a approximately 200 MeV/c up to ~15 GeV/c.

FEMC The forward ECal (FEMC) will be a Pb-Scintillator shashlik calorimeter. Its towers have an active depth of 37.5cm with an additional 5cm readout space. Each tower consists out of 66 layers of alternating 1 cm×1 cm×0.16 cm Pb and 1 cm×1 cm×0.4 cm scintillator.

LFHCAL The forward HCal (LFHCAL) is a steel-tungsten-scintillator calorimeter. Its towers have an

Table 1: Key detector requirements for ECCE central detector, with associated challenges, and a brief description of the ECCE approach to address each issue.

Topic	Challenge	ECCE solution	Comment
Hermetic e^- coverage	Leave no gaps in e^- EMcal coverage while also folding in PID/hpDIRC readout needs	hpDIRC readout in backward region; Moved EEMC inward as much as possible; Extend BEMC longitudinally	Good coverage for negative rapidity; performance verified with full simulations
Momentum resolution in forward/backward regions at high η	Achieve YR requirements with a realistic tracker including support materials in the BaBar solenoid	Five ITS3 Si disks forward and four disks backward; Additional AC-LGAD tracking before (after) dRICH (mRICH)	Used AI optimization. Upgrade option: AC-LGAD ring in forward region behind dRICH for η = 3–3.5
Backward Particle Identification	Constrained space to maximize EMCal coverage	AC-LGAD TOF for low-momentum; mRICH for hadron PID	mRICH is a space-efficient solution
Backward e^- PID, π^- suppression up to 10^{-4}	Highest precision EM calorimetry	Use all $PbWO_4$	Can separate out EMCal to reach beyond $\eta = -3.4$
Barrel PID – e/π separation up to 10^{-2}–10^{-4}, down to 0.2 GeV/c	Need good EMcal resolution; need additional e/π below 2 GeV/c	55 cm long SciGlass towers for high precision EMcal; hpDIRC for π veto down to p = 0.3 GeV/c; AC-LGAD TOF for $p \leq 0.4$ GeV.	Leave 4 cm for μRWELL between hpDIRC and EMCal to seed PID performance of hpDIRC and improve tacking resolution
Barrel PID – $\pi/K/p$ separation down to 0.2 GeV/c	hpDIRC only covers down to 0.6 GeV/c	AC-LGAD TOF for 0.2 <p <0.6 GeV/c	μRWELL directly after hpDIRC to increase performance.
Barrel Tracking resolution	Achieve YR requirements with a realistic tracker including support materials in the BaBar solenoid	Three ITS3 Si vertex and two Si sagitta layers followed by two μRWELL, AC-LGAD, and far outer μRWELL layer;	Used AI optimization of tracker and support system layout
Forward Hadronic calorimetry	Jet energy resolution <50%/ $\sqrt{E}$	Longitudinally separated calorimeter to meet needs in high-η region.	Upgrade Option: Dual Calorimeter (or only central in region of highest need)
Forward Particle Identification	Constrained space in forward region	AC-LGAD TOF for low- momentum; dRICH for high- momentum (C_4F_{10} based)	Seed dRICH ring finder with AC-LGAD before dRICH; Employ recirculation and gas recovery systems for environmentally unfriendly gas use.

active depth of 1.4 m with an additional space for the readout of about 20-30 cm depending on their radial position. Each tower consists out of 120 layers of alternating 5cm x 5cm x 1.6cm steel and 5cm x 5cm x 0.4cm scintillator material and 20 layers of alternating tungsten and scintillator material of the same size. In each scintillator a loop of wavelength shifting fiber is embedded. Ten consecutive fibers in a tower are read-out by a single silicon photo multiplier, leading to 7 samples per tower, with the last 10 layers acting as tailcatcher.

Far-forward detectors The auxiliary detectors consist of a set of trackers and calorimeters that are closely integrated with the beam-line elements. The detector are designed to measure very forward particles to high precision with a high rejection of beam-related background. The far forward detection systems consist of the following components:

B0 spectrometer The B0 spectrometer measures charged particles and photons at forward ($\eta > 3$) angles to facilitate studies of exclusive processes and general process characterization. This subsystem is designed for reconstructing charged particles with angles of $5.5 < \theta < 20.0$ mrad, and also large angle protons from nuclear breakup. The B0 detector is embedded in the first dipole magnet after the interaction point (B0pf). It consists of four layers of AC-LGAD tracking planes followed by an array of $PbWO_4$ crystals for the photon detection. The $PbWO_4$ array consists of 250 crystals, each 10 cm long with a surface area of 2x2 cm^2.

Zero-Degree Calorimeter The ZDC consists of a single unit with four different calorimeter layers.

- $PbWO_4$ Crystal calorimeter: This is a silicon pixel layer plus a layer of $PbWO_4$ crystals intended to measure low energy photons. In front of the crystal layer, a silicon pixel layer is attached.
- W/Si sampling calorimeter: This is an ALICE FoCal-E style calorimeter [14] and consists of alternating tungsten plates and silicon sensor planes. It is meant to measure the residual photon energy escaping the $PbWO_4$ Crystals in the shower development of high-energy photons and neutrons.
- Pb/Si sampling calorimeter: This is a calorime-

Table 2: ECCE Detector Far-Forward/Far-Backward requirements

Topic	Challenge	ECCE solution	Comment
Far-Backward – Low-Q^2 Tagger	Measure low-Q^2 photo-production with as minimal a Q^2-gap as possible.	Spectrometer with AC-LGAD tracking and $PbWO_4$ calorimetry	
Far-Backward – Luminosity Detector	e-ion collision luminosity to better than 1% and relative Luminosity for spin asymmetries to 10^{-4}	Zero Degree Calorimeter with x-ray absorber and e^+/e^- pair spectrometer with AC-LGAD tracking and $PbWO_4$ calorimetry	two complementary detection systems
Far-Forward – B0 Spectrometer	$\eta > 4$ charged particle tracking and γ measurement	Four Si trackers with 10 cm $PbWO_4$ calorimeter	
Far-Forward – Off-momentum Detectors	forward particles (Δ, Λ, Σ, etc) decay product measurement	AC-LGAD detectors	Sensors on one side detect p, on other side p^- from Λ decay; sensors outside beam pipe
Far-Forward – Roman Pots	Detect low-p_T forward-going particles	AC-LGAD detectors	fast timing (~35 ps) removes vertex smearing effects from crab rotation; 10σ from beam
Far-Forward – Zero-degree Calorimeter	Measure forward-going neutrons γ and heavy-ion fission product	FOCAL-type calorimeter with high-precision EM and Hadron Calorimetry	Upgrade option: AC-LGAD layer to capture very high rapidity charged tracks

ter with 3 cm-thick lead plane absorbers and active silicon pad layers, where the pad-layer design is as in the W/Si calorimeter.

- Pb/Sci. sampling calorimeter: This is to measure hadron shower energy and uses 3 cm thick lead plane absorbers with 2 mm-thick scintillator planes as active materials. The calorimeter is segmented as 10 cm x 10 cm on a plane and 15 layers of scintillator planes will be read together, making a tower.

Far-backward detectors The auxiliary far-backward detectors consist of a low-Q^2 tagger and a luminosity monitor.

Low-Q^2 tagger The tagging system is made up of two detection systems which are located at different distances from the beam, each including two AC-LGAD tracking layers followed by a high-resolution $PbWO_4$ calorimeter.

Luminosity monitor A forward $PbWO_4$ calorimeter with a passive x-ray absorber and a two-arm e^+/e^- pair spectrometer measures the beam luminosity. Each includes AC-LGAD tracking layers and a high-resolution $PbWO_4$ calorimeter.

Electronics/DAQ The ECCE DAQ is a fully streaming readout (SRO) design capable of supporting high bandwidth to the Event Buffer and Data Compressor (EBDC) computers as well as high bandwidth to the data storage. A key component of this design is the Data Aggregation Module (DAM), for which we take as the current model the ATLAS FELIX board that will be used by sPHENIX in their hybrid streaming DAQ. We assume the development of a specific iteration of a FELIX-like board [15] as the DAM board for ECCE (also referred to as "EIC-FELIX" in the text that follows) that will serve as a common interface for all of the subsystems. The use of a common interface reduces the number of electronics designs that need to be verified and supported in the experiment.

The general design of the ECCE data acquisition builds on the sPHENIX DAQ system, which already demonstrates almost all of the concepts of the envisioned ECCE DAQ system. However, while sPHENIX had to be a hybrid of triggered and streaming readout components, the ECCE DAQ will be built around a trigger-less Streaming Readout (SRO) concept, similar to the streaming readout systems currently in use at JLab and in the ALICE experiment at the LHC.

Computing The ECCE computing will be based on a distributed model with multiple sites for calibration, storage and analysis. Computing resources must be sufficient to do calibrations and reconstruction in near real-time. Disk space should be sufficient for holding up to 3 weeks to allow time for data quality checks. Tape storage will used for long term backup of the filtered data.

Figure 3 shows the material distribution of the ECCE central detector via a radiation length scan of the detailed ECCE GEANT4 model. The large acceptance and low mass inner tracker (green) is hermetically enclosed by the PID detectors (red and yellow) and EM calorimetry (blue). Hadronic calorimeters further cover $\eta > -1.1$.

3. Magnet

ECCE plans to reuse the BaBar/sPHENIX solenoid and the surrounding combined hadronic calorimetry and flux containment system for the magnet.

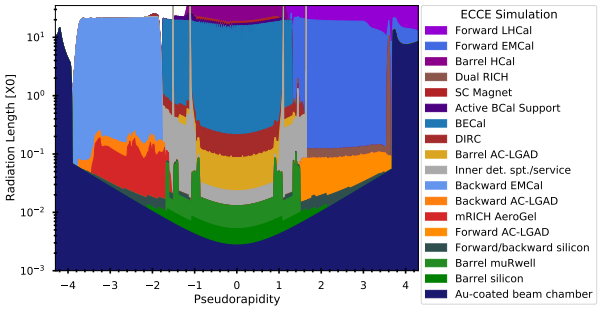

Figure 3: The stacked plot of material distribution in the ECCE detector subsystems, which is quantified as the radiation length that photons from the central interaction point observe and is averaged over azimuth.

Table 3: Design parameters of the BaBar superconducting solenoid.

Central Induction	1.5 T* (1.4 T in ECCE flux return)
Conductor Peak Field	2.3 T
Winding structure	Two layers, graded current density
Uniformity in tracking region	±3%
Winding Length	3512 mm *at R.T.*
Winding mean radius	1530 mm *at R.T.*
Operating Current	4596 A (4650 A*)
Inductance	2.57 H (2.56 H*)
Stored Energy	27 MJ
Total Turns	1067
Total Length of Conductor	10,300 m

* Design Value

The magnet for the BaBar experiment at PEP-II at SLAC was manufactured by Ansaldo in 1997 and commissioned in 1998. It was transferred to BNL in 2015 for use in the sPHENIX experiment and passed an initial high-field test (up to 1.3 T) in 2018. Its main design parameters are listed in Table 3. For an EIC detector the region covered by the barrel detectors should span a pseudo-rapidity $-1 < \eta < 1$, corresponding to an angle of ~40 degrees. This corresponds well with the BaBar solenoid, which has a warm bore diameter of 2.84 meters and a coil length of 3.512 meters, corresponding to a 39 degree angle.

The reuse of the BaBar solenoid for the EIC was the subject of an engineering study and risk analysis in 2020 [13]. The main conclusion of the assessment was that the "magnet should be suitable for prolonged use as part of the detector system for the EIC project." The report also suggested the implementation of several maintenance and improvement modifications, including new protection circuits such as voltage taps, inspection and, as needed, reinforcement of the internal mechanical support, including new strain gauges, and replacement of control instrumentation sensors. The implementation of some of these suggestions would involve opening the magnet cryostat, which could create additional risk of magnet failure. In 2021 JLab engineers revisited the risk analysis and, following extensive discussions, decided that any modifications or refurbishment that require opening the BaBar solenoid cryostat would not be worth the additional risk [16]. They further noted that no such actions will be necessary if the magnet continues to operate well throughout a high-field magnet test with the sPHENIX

Figure 4: The BaBar solenoid in late February 2022, during installation in the sPHENIX experiment. The solenoid is surrounded by the barrel outer hadronic calorimeter and flux return. The barrel flux return (outer hadronic calorimeter) and BaBar solenoid are items planned to be reused by the ECCE experiment. The experimental cradle may also be reused.

experiment flux return (which will also be re-used for ECCE) in mid-2022 and subsequent initial sPHENIX experimental operations starting from 2023 until 2025.

Further magnet engineering studies of the ECCE detector magnet indicate that the unbalanced forces on the magnet are small, a net force of 4kN or less than 1000 lbs, because the magnetic field at the locations of the ECCE forward and backward calorimeters are small and most of the magnetic flux is returned through the barrel. These small forces should not present a substantial engineering difficulty in the proposed ECCE configuration.

The scope of the reuse of the BaBar solenoid in ECCE includes a review by a panel of experts (following initial sPHENIX running), the disconnect of the magnet in IP-8 and move to IP-6, a new valve box, and assembly and magnet mapping in IP-6. The risk mitigation strategy associated with the reuse of the BaBar solenoid, including the design of a potential replacement magnet, are discussed in Section 11.

4. Tracking

ECCE features a hybrid tracking detector design (Figure 5) using three state-of-the-art technologies to achieve high precision primary and decay vertex determination, as well as, excellent tracking momentum and distance of closest approach res-

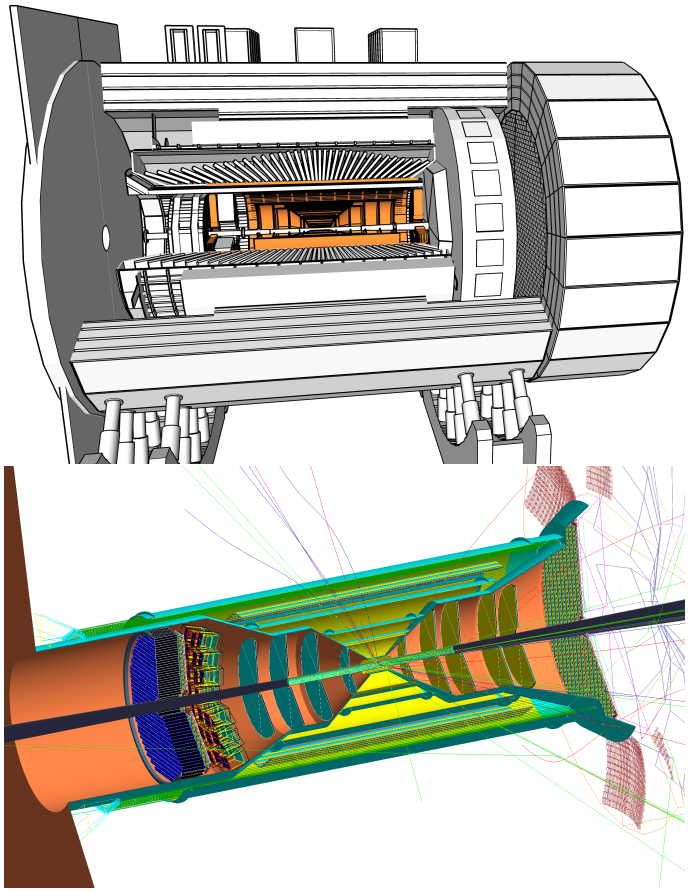

Figure 5: Tracking system of ECCE in mechanical model (top) and GEANT4 simulation (bottom). The tracking system is tightly integrated with the PID detectors which is also shown on the right. Support and cabling for the these detectors was implemented (copper-colored cylinder-cone) to count for its material and acceptance effects.

olution in the $|\eta| \leq 3.5$ region with full azimuth coverage [17]. The ECCE tracking detector consists of the Monolithic Active Pixel Sensor (MAPS) based silicon vertex/tracking subsystem, the μRWELL tracking subsystem and the AC-LGAD outer tracker, which also serves as the ToF detector. The ECCE tracking design has been optimized assisted by Artificial Intelligence (AI) taking into account BaBar magnet coverage, integration with the other detector subsystems, and cost.

The tracker geometry is shown in schematic form in Fig. 6 which displays the detector in the $R-z$ plane. The barrel layers centered at $z = 0$ have a cylindrical geometry, while the endcap layers centered at $R = 0$ are disks oriented around the z axis. The MAPS silicon detector contains 3-layer silicon vertex layers, 2-layer silicon sagitta layers, five disks in the hadron endcap and four disks in the electron endcap region. This silicon vertex/tracking detector provides the desired primary vertex and displaced vertex reconstruction also documented in the EIC yellow report [2] and the tracking momentum and DCA_{2D} resolutions (see Fig. 8 and Fig. 9) for heavy flavor measurements. For the barrel layers at large radii, which have the largest surface area, cylindrical μRWELL gas trackers are used to optimize performance at reduced overall cost. These are introduced both right outside the Si tracker and in front of the barrel EM calorimeter. In addition, an AC-LGAD based ToF layer in each section provides a precision space-time measurement on each track. The tracking system is thus tightly integrated with the PID detectors.

4.1. MAPS

The silicon vertex and sagitta layers utilize MAPS technology, as implemented in high-precision (10 μm pixel pitch and $\sigma_{xy} = 2.9$ μm) low-material (0.05%/layer) ALICE-ITS-3-type sensors [18, 19], used in both cylindrical and disk configurations.

The MAPS detector systems have been costed based on the TowerJazz 65nm production line. This technology is in the prototype sensor design and characterization stage. Recent R&D on the ITS-3 has delivered a 32 by 32 pixel matrix prototype sensor using the 65nm production line that is undergoing beam test studies at CERN. Validation of the curved ALPIDE (ITS-3) sensor performance was obtained by early beam test results. The mechanical design for the silicon tracking detector, especially for the stave and disk layout and assembly, is led by the ongoing EIC R&D project eRD111. Reduction of the material budgets for the EIC silicon tracking detector service parts is also being studied as part of the EIC eRD104 project. Alternative silicon technologies have been explored such as the Depleted MAPS (DMAPS), and progress in the MALTA DMAPS technology has been reported in [20]. All these R&D activities align with other major project upgrades or construction projects such as the ALICE ITS-3 upgrade. The required sensor R&D is included in the ECCE detector R&D plan.

4.2. μRWELL

In ECCE μRWELL layers will form three barrel tracking layers further out from the beam-pipe than the silicon layers. The barrel gas tracker layers include two inner barrel μRWELL layers, as well as a single outer barrel μRWELL. The μRWELL technology is a single-stage amplification Micro Pattern Gaseous Detector (MPGD) that is a derivative of Gas Electron Multiplier (GEM) technology. It features a single kapton foil with GEM-like conical holes that are closed off at the bottom by gluing the kapton foil to a readout structure to form a microscopic *well* structure. The technology shares similar performances to GEM detectors in term of rate capability, while providing a better spatial resolution than GEM. Furthermore, compared to GEMs, μRWELL has distinct advantages of flexibility, more convenient fabrication and lower production cost making it the ideal candidate for large detectors. Large area μRWELL foils have already been developed and manufactured at CERN. All μRWELL detectors will have 2D strip based readout. The strip pitch for all three layers will be 400 μm. Figure 7 shows the resolution results from a μRWELL prototype detector in test beam at Fermilab (June-July 2018) as part of the EIC eRD-6 activities. The measurements were done using a beam hitting the detector perpendicularly, and using detailed MC simulations we estimate a 55μm resolution for a curved geometry where the particle hits the detector at an angle.

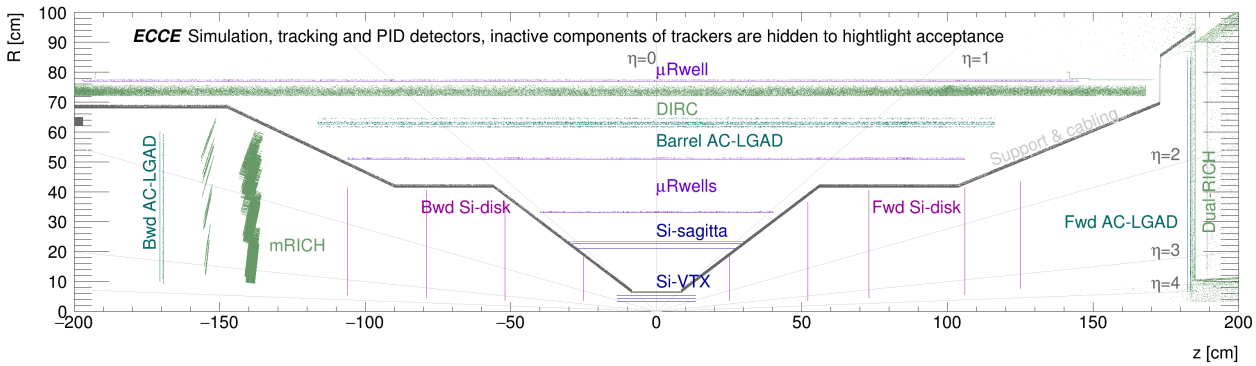

Figure 6: Schematic view of the ECCE tracker, including silicon, μRWELL, AC-LGAD, DIRC, mRICH and dRICH detector systems. **Need better version of this image.**

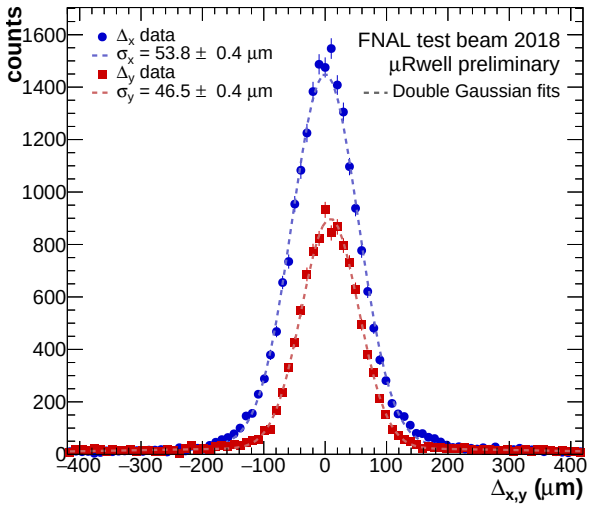

Figure 7: Preliminary results of spatial resolution performances of the μRWELL prototype with 2D X-Y strip readout layer.

The Korean institutions in the ECCE collaboration will manufacture the μRWELL foils for the ECCE μRWELL detectors. Specifically, a Korean manufacturer (Mecaro) has demonstrated that they can produce high quality large MPGD foils for the CMS detector at the LHC, working in conjunction with member institutions of the Korean ECCE collaboration. In addition, Chinese institutions in the ECCE collaboration have experience with the DLC resistive coating required for μRWELL detectors.

4.3. AI optimization

A framework for Multi-Objective Optimization (MOO) has been incorporated into the ECCE detector design simulation. AI has played a crucial role in choosing the combination of technologies for the inner tracker. The choice of having ITS-3 and the μRWELL gas tracking layers, as well as the disk minimum radii were supported by AI. This has been an iterative process that evolved over time and required interplay between the ECCE teams working on Physics, Detector and Computing.

Our approach deals with a complex optimization in a multidimensional design space driven by multiple objectives that encode the detector performance, while satisfying several mechanical constraints. This framework has been developed for the optimization of the inner tracker of ECCE and can in principle be extended to another sub-detector or to a system of sub-detectors, provided a viable parametrization of the detector simulation can be produced. Different parametrizations of the inner tracker design have been explored and most of our studies have been characterized by at least 11 parameters in the design space characterizing the location of the tracking layers in the central region and the disks in the two endcaps. The parametrization has been extended to include the support structure in the design optimization process and more recently to the outer tracking layers. The different designs have been optimized with particle gun samples of pions and then studied and validated with independent data samples and physics analyses. At least three objective functions have been optimized simultaneously. In particular, for a 3-objective problem we utilized the momentum resolution, the polar angular resolution along with the Kalman filter efficiency of π tracks. This problem has been tackled with evolutionary algorithms to assist the design during the detector proposal. A recently developed framework for MOO, PYMOO [21], has been implemented which supports algorithms like NSGA-II and NSGA-III [22] and distributed evaluation with task scheduler like DASK [23].

This approach accommodated both mechanical and geometrical constraints during the optimization process. In our studies we included at least 5 constraints (*e.g.*, the outermost location as well as the difference between the outer and inner radius of a disk, or the radius of the outermost layer in the inner tracker). Overlaps in the design are excluded by a combination of constraints, ranges for the exploration of the parameters and internal checks done before and during the entire optimization process. Further details can be found in [24].

The AI-assisted design has been used as input to multiple iterations of the ECCE tracker design, which led to the current tracker layout [17] (Fig. 5 and 6), and is also contributing to the ongoing project R&D to reduce the impact of readout and services on the tracking resolution as discussed in Section 4.6.

4.4. Expected backgrounds

Vacuum and background estimates were done in joint working group meetings across both the ATHENA and ECCE protocollaborations. A detailed simulation study was carried out

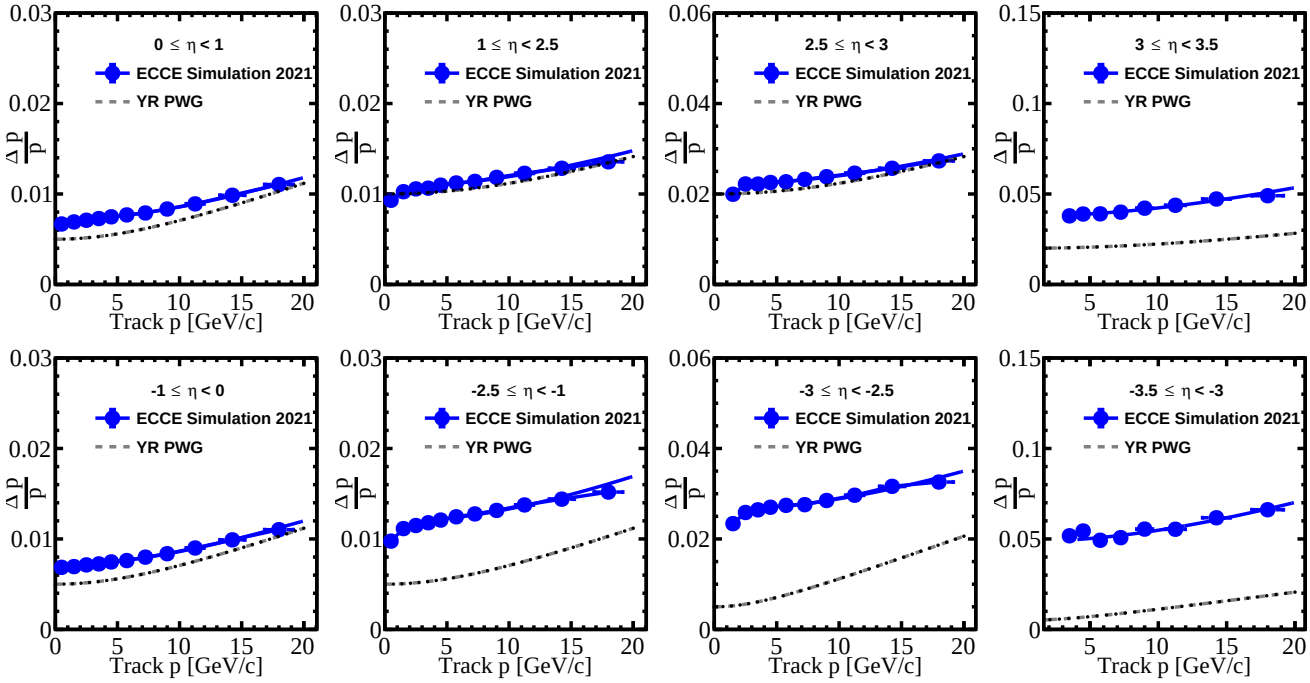

Figure 8: ECCE pion track momentum resolution (data points) with the EIC YR PWG requirements for the tracker indicated by the dashed lines. Note that the ECCE performance simulations take into account materials for readout and services. The impact of these can be observed most clearly in the bins covering the barrel/barrel endcap transition regions. As an integrated EIC detector with all subsystems operating in a complementary way, ECCE achieves the EIC physics goals.

to assess the collision signal and background from beam gas and synchrotron radiation on tracking detectors in the BaBar magnetic field [25]. Although the beam gas background was found to be small, the synchrotron radiation on the MAPS-based silicon trackers can be very significant and its uncertainty is large at this stage of the EIC design. A high-Z coating in the Be-section of the beam pipe (e.g. 2 μm Au coating) was shown to reduce the synchrotron hit rate in the silicon vertex tracker by four orders of magnitude resulting in a manageable hit rate [25, 26]. Therefore, all ECCE studies adopted such synchrotron shielding coating which introduces 0.06% X_0 (at $\eta = 0$) of additional material to the beam pipe ($\sim$ 30% relative increase).

4.5. Tracking performance

The performance of the ECCE reference tracker design has been studied using single pions propagated through the ECCE GEANT4 simulation framework. The momentum resolution is presented in Fig. 8 together with the YR requirement indicated as the dash lines. In the region, $-1 < \eta < 3$, the ECCE momentum resolution is consistent with Yellow Report physics requirements [2]. Between $1 < \eta < 1.5$ a substantial deviation is observed that is not obvious in Figure 8. This difference is expected from the material for readout and services (copper-colored structure in right of Figure 5), whose impact is largest in this region. Further AI-assisted optimization in this region is on-going as discussed in Section 4.6.

In the backward region $\eta < -1.0$ and in the most forward bin the ECCE momentum resolution provided by tracking exceeds the YR requirements [2]. However, ECCE is an integrated detector and in this region the physics performance, and in particular for $\eta < -2.5$, is achieved through excellent EM calorimetry. Due to the limited time since the call for proposals to produce and analyze complete GEANT4 simulations for physics performance, many of the physics studies used only tracking. Nevertheless, these studies all show sufficient performance for the EIC physics program. The addition of the calorimetry information will only improve these results, as shown for key physics topics.

We further note the dominant YR requirement for the momentum resolution in the backward region is driven by coherent J/ψ production on the nuclei, and in particular the t-reconstruction from the forward particles. Nonetheless, the ECCE physics studies have shown that for either a 1.4 T or even a 3.0 T field strengths the t-reconstruction resolution is dominated by the calorimeter.

The resolution of measurements of distance-of-closest-approach (DCA_{2D}), which is critical for heavy flavor measurements, is provided in Fig. 9 and also compared with YR requirement. The ECCE DCA resolution is consistent with the YR, and will enable robust physics programs in heavy flavor measurements and beyond standard model search.

4.6. Ongoing R&D for support structure optimization

Given the importance of the service structure in the tracking detector, the reduction of the impact of readout and services on tracking resolution is subject of ongoing R&D and ECCE has made tremendous progress on this front using AI. The AI investigation in the ECCE framework focused on optimizing the

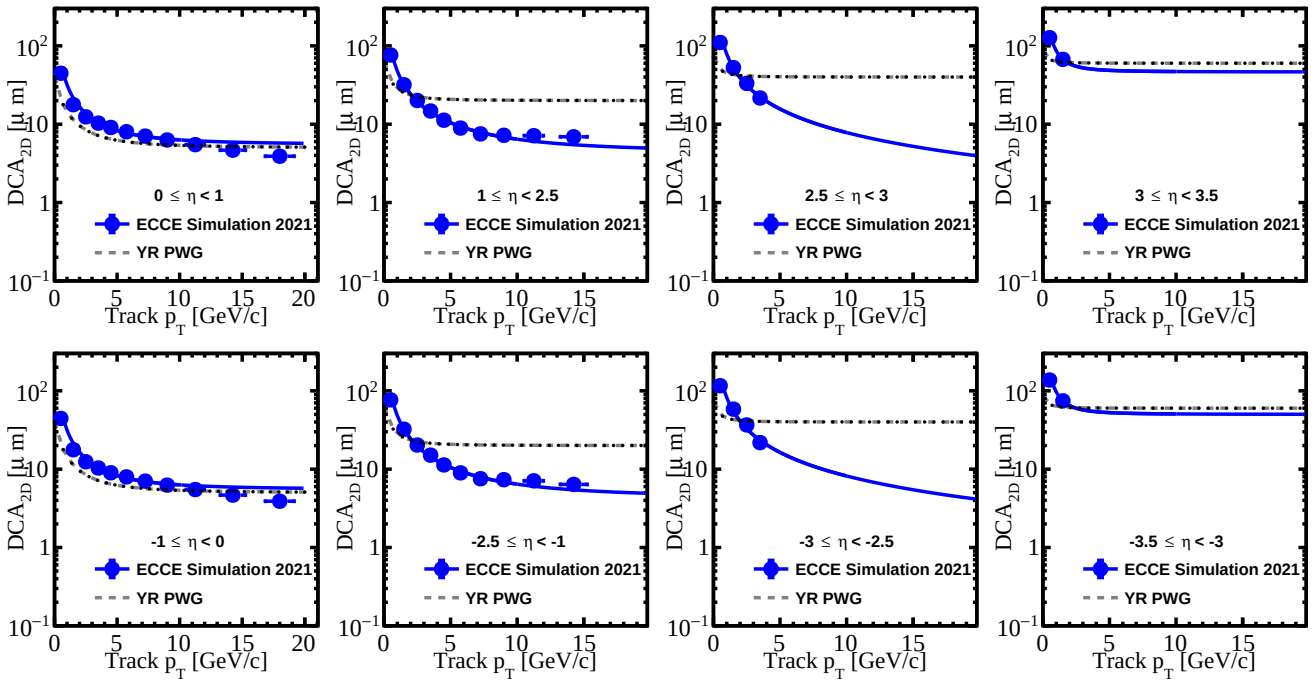

Figure 9: Pion DCA$_{2D}$ resolutions (data points), which is compared to the EIC YR PWG requirement (dashed lines). The ECCE DCA resolution is consistent with YR requirements.

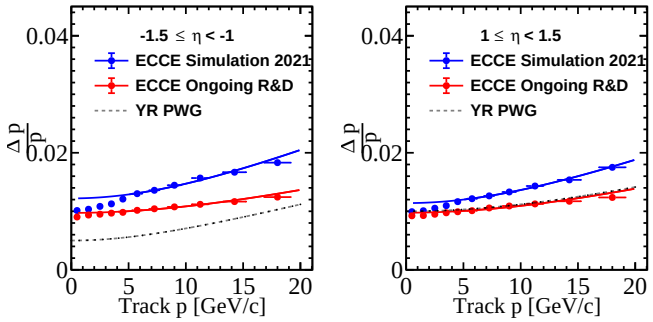

Figure 10: The momentum dependence of the tracker momentum resolution for the ECCE reference tracker design (ECCE Simulation, blue solid circles) and for the projective mechanical support design of the ECCE ongoing project R&D that will continue after the proposal (red solid circles). The latter shows a reduction of the impact of readout and services on the tracking resolution. Note that the backward region (left panel) relies on the EM calorimeter, and thus a resolution larger than the EIC YR PWG requirement is acceptable.

tracker design with a projective support cone structure that reduces the amount of material a particle traverses. The design concept is illustrated in the Tracking document [17] and more details on the AI based studies can be found in [24]. The momentum resolutions resulting from this investigation are shown in Fig. 10. The largest impact is in the region between the central barrel and endcaps ($1 < \eta < 1.5$ and $-1.5 < \eta < -1$) while the tracking momentum resolution in the central barrel as well as at large pseudo-rapidities ($|\eta| > 1.5$) is largely unaffected.

5. Particle Identification

The ability to identify hadrons in the final state is a key requirement for the physics program of the EIC. Being able to tag the flavor of the struck quark in semi-inclusive DIS can, for instance, provide valuable information about the transverse momentum distributions (and potentially orbital angular momentum) of the strange sea quark, while open charm (with subsequent decays into kaons) is important for probing the distribution of gluons in protons and nuclei.

The choice of ECCE PID detector technologies was based on the outcome of the EIC generic R&D program (eRD14 EIC PID Consortium and eRD29 on TOF with the LGADs technology), started in 2015, and in line with the baseline EIC detector concept in the Yellow Report (YR) [2]. The longitudinally compact, modular RICH (mRICH), the radially thin high-performance DIRC (hpDIRC), the dual-radiator RICH (dRICH), and AC-LGADs based TOF, provide excellent PID over a wide momentum range for the full final state phase space [27]. The geometries of all PID detectors were optimized to fit the ECCE baseline design while maintaining the required performance. Figure 11 (left) shows the four PID systems in a 3D model of the ECCE detector and (right) their π/K separation coverage as a function of momentum and pseudo-rapidity for a sample of physics events. Compared to the YR reference detector, a number of key design features of the PID systems were optimized for ECCE.

The expected PID performance of the three ECCE Cherenkov detectors was obtained from standalone GEANT4 simulation and analytical calculations, parametrized and used as input into the ECCE physics studies. Figure 12 shows the

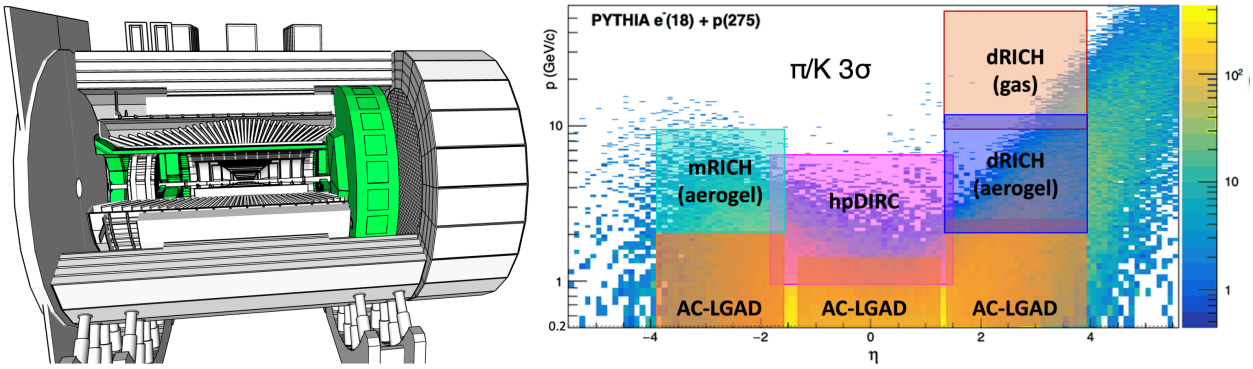

Figure 11: Left: 3D model of the ECCE detector with the PID systems highlighted. Right: Expected 3 standard deviations π/K separation coverage for the ECCE PID systems as a function of the particle momentum and pseudo-rapidity. Full coverage is achieved by making use of the veto mode of the Cherenkov detectors, complementing the TOF PID in the low momentum region.

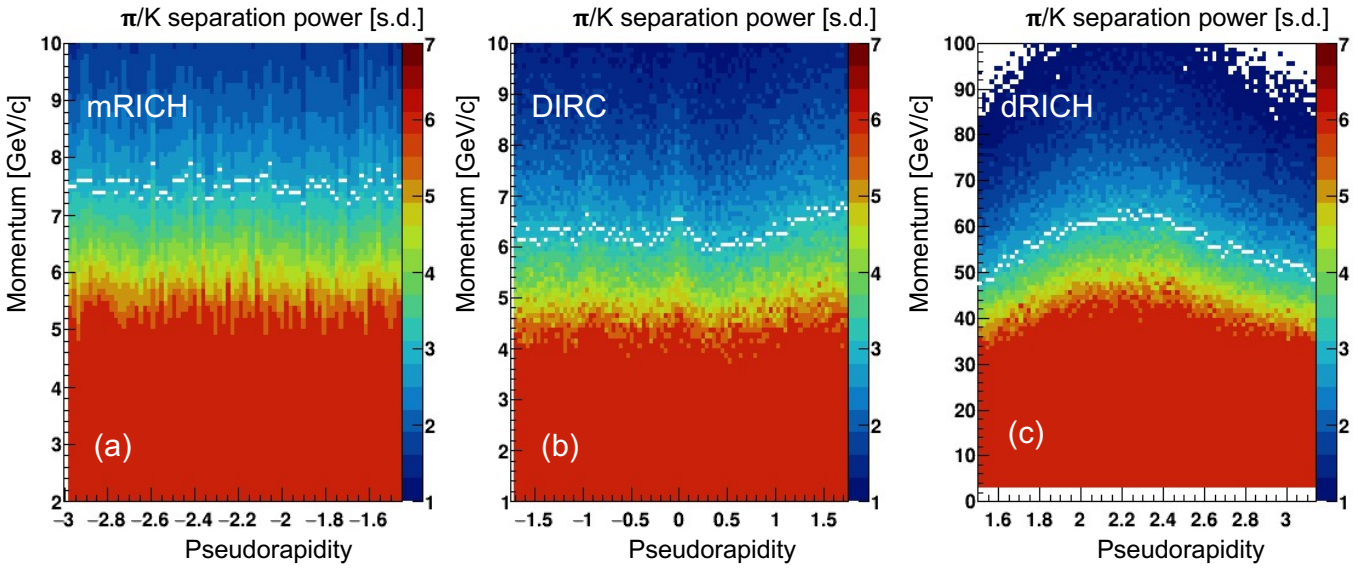

Figure 12: Parametrized π/K separation power in ECCE as a function of particle momentum and pseudo-rapidity for mRICH (a), hpDIRC (b), and dRICH (c) based on standalone full GEANT4 simulation and analytical calculation. The white symbol marks the maximum momentum for 3 standard deviations π/K separation in each pseudo-rapidity bin.

parametrized π/K separation power in units of the number of standard deviations as a function of pseudo-rapidity and momentum for conservative assumptions for the tracking angular resolution.

Note that subsequent tuning of the PID detector geometries and reconstruction algorithms resulted in further improvement of the PID performance, which are not reflected in the shown parametrization. The resulting momentum coverage for the separation of e/π, π/K, and K/p with three standard deviations or more is summarized in Table 4 for the three ECCE Cherenkov systems. The Cherenkov system performance is further separated into the nominal "Ring Imaging" mode of operation, which provides positive ID of the particle type, and the so-called "threshold mode" or "veto mode", which uses the number of Cherenkov photons in excess of the expected background to differentiate between particle types above or below the threshold for Cherenkov light emission. The combined performance of the ECCE Cherenkov detectors meets or exceeds the ECCE PID requirements.

Table 4: Summary of the PID performance of the ECCE Cherenkov systems (momentum coverage in GeV/c).

PID	Mode	mRICH	hpDIRC	dRICH	
				aerogel	gas
π/K	Ring Imaging	2 – 9	1 – 7	2 – 13	12 – 50
	Threshold	0.6 – 2	0.3 – 1	0.7 – 2	3.5 – 12
e/π	Ring Imaging	0.6 – 2.5	< 1.2	0.6 – 13	3.5 – 15
	Threshold	< 0.6	–	< 0.6	< 3.5

The Cherenkov systems provide, in addition to hadron PID, a significant contribution to the e/π identification. When combined with the EM calorimeter, the mRICH and hpDIRC will provide excellent suppression of the low-momentum charged-pion backgrounds, which otherwise limit the ability of the EM-

Cal to measure the scattered electron in kinematics where it loses most of its energy. The time-of-flight (TOF) system, using the AC-LGAD technology, will provide hadronic PID and electron identification in the momentum range below the thresholds of the Cherenkov detectors and provide a time resolution of 25 ps and a position resolution of about 30 μm over a nearly 4π coverage.

Figure 13 shows the realistic ECCE magnetic field with highlighted PID detectors envelopes. In the region of the hpDIRC detector plane, where the MCP-PMTs will be located, the magnetic field is at a level of 0.3–0.4 T, which provides a large safety margin in terms of the MCP-PMT field tolerance. Both RICH detectors in ECCE assume the use of SiPM, which are insensitive to magnetic fields of this strength, as their baseline photosensor. Bending of the charged particle tracks in RICH detectors can potentially have an impact on performance, but studies of the deviation of charged tracks from a straight line within the gas volume of the dRICH show a negligible impact on performance.

5.1. mRICH

The novel design of the modular RICH (mRICH) modules consists of four components. A block of aerogel serves as the Cherenkov radiator, immediately followed by an acrylic Fresnel lens, which focuses the ring image and acts as a UV filter. A pixelated optical sensor is located in the image plane, and flat mirrors form the sides of each mRICH module.

Several optimizations of the ECCE mRICH design were made compared to the YR reference detector: (1) the projective array design was optimized maximizing the acceptance, removing the polar-angle dependence, and reducing the material budget; (2) the dead region between the mRICH modules is minimized using optimized thin module walls and mirrors (shorter as well) (3) an integrated mRICH array mechanical design was designed, consistent with the simulated array configuration in GEANT4.

To study the performance of mRICH setup in ECCE, a set of tracks from the most demanding parts of the phase space were used, where the performance is expected to deteriorate, setting a lower limit on the performance and comparing it to what we see from the parametrizations. The study specifically focuses on the cases where the particles are incident at the surface of the aerogel closer to the outer edges with an outward angles and tracking angular resolution of 2.5 mrad. Fig. 14 shows the results for the e/π and π/K separation. The dips in the π/K separation at 2 and 3.8 GeV/c are due to the Cherenkov thresholds for kaons and protons in the aerogel. The obtained results show better performance than that used in the parametrization, shown in Fig. 12a, which indicates a better momentum reach once the mRICH reconstruction is further optimized.

5.2. hpDIRC

The radially-compact hpDIRC is based on a fast focusing DIRC design. Thin rectangular bars, made of synthetic fused silica, serve as Cherenkov radiators and guide the photons to the readout section where they are focused by a lens and recorded by an array of pixelated photon sensors, placed on the back surface of a fused silica prism expansion volume. Key features of the hpDIRC include three-layer spherical lenses, photosensors with small (3 mm×3 mm) pixels, and fast readout electronics.

Compared to the YR reference detector, several hpDIRC design aspects were optimized for ECCE. The expansion volume and readout were moved from the hadron side to the electron side for better detector integration and to minimize gaps in the EM calorimeter coverage. The bar box radius was decreased to match the EM calorimeter barrel size and the number of bar boxes, as well as the number of bars per bar box, were tuned to optimize the azimuthal coverage of the hpDIRC and to be consistent with the reuse of the BaBar DIRC bars. None of these changes had a significant impact on the performance of the hpDIRC.

Figure 15 shows the hpDIRC geometry as well as and the expected performance of the hpDIRC from the standalone GEANT4 simulation studies for two particular cases. The black points show the separation power for charged pions and kaons as a function of the polar angle at a momentum of 6 GeV/c while the red points show the same quantity for charged pions and electrons at 1.2 GeV/c. The expected particle identification performance of the hpDIRC exceeds the ECCE PID goal of three standard deviation separation power for e/π up to 1.2 GeV/c and π/K up to 6 GeV/c for the entire polar angle range.

5.3. dRICH

The dual-radiator Ring Imaging Cherenkov (dRICH) detector configuration for ECCE consists of six identical, transversely open sectors. Each contains two radiators (aerogel and C_2F_6 gas), sharing the same outward focusing mirror and readout planes, which are instrumented with highly segmented photosensors (3 mm×3 mm pixels), located outside of charged particle acceptance. The photosensor tiles are arranged on a curved surface to compensate for aberrations. Due to the open geometry of the dRICH sectors, photons from a Cherenkov cone may split over two or more sectors Relative to the YR reference detector, the ECCE dRICH radial size was scaled down by 25% to fit into the envelope defined by the HCAL. It was also moved about 40 cm closer towards the IP to maintain the original acceptance.

Figure 16 shows the preliminary results of the dRICH K/π separation power for three incidence angles and selected momenta. The results are obtained from the full ECCE simulation framework with the realistic magnetic field map and conservative tracking resolution. Note that the simulated design uses a simplified flat detector plane and that the mirror curvature is not fully optimized yet. The results are in good agreement with expectations and already reach the desired 3 standard deviations or more over almost the full required momentum range. Further improvement of the dRICH performance is expected once the planned AI-based geometry optimization is completed.

5.4. AC-LGAD-based TOF

The AC-LGAD TOF technology is based on a simple p–n diode concept [28], where the diode is fabricated on a thin high-resistivity p-type silicon substrate. A highly-doped p–layer (the

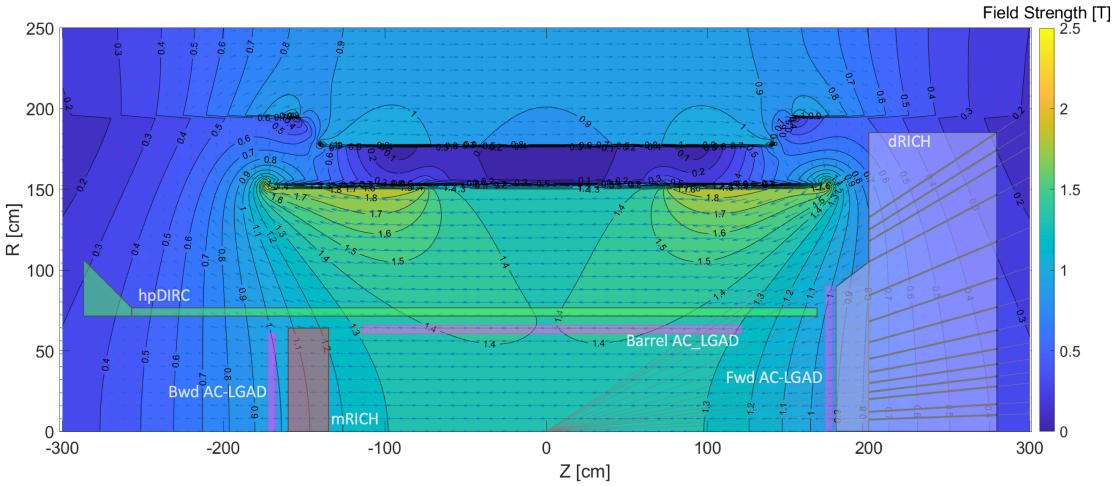

Figure 13: ECCE magnetic field map with the PID detector envelopes overlaid.

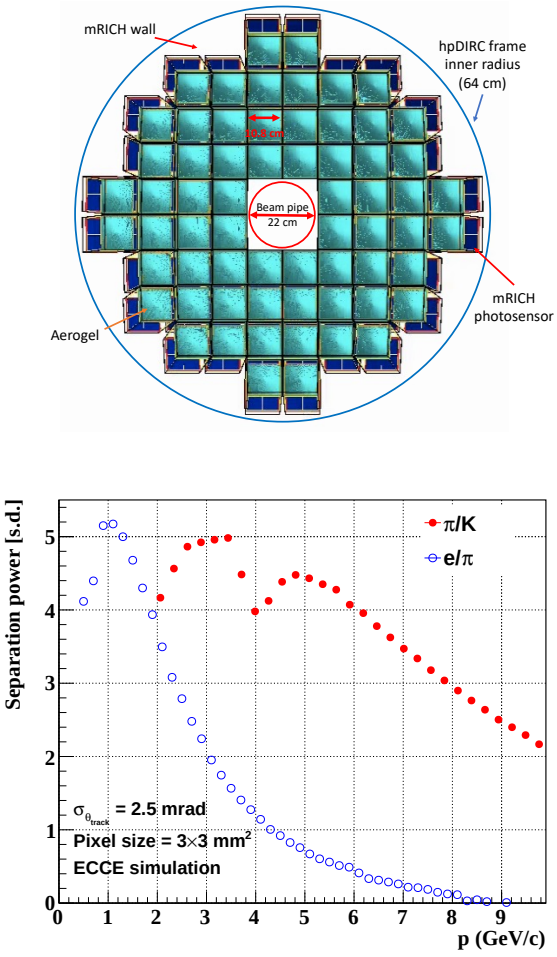

Figure 14: Top: Front view of mRICH module array in the allocated space projected towards the IP. Bottom: The separation power of the mRICH in units of number of standard deviations as function of particle momentum from ECCE simulation.

Table 5: Summary of the Momentum coverage in GeV/c of the ECCE Time-of-Flight detector in corresponding regions.

PID	ETTL	CTTL	FTTL
e/π	< 0.5	< 0.45	< 0.6
π/K	< 2.1	< 1.3	< 2.2
K/p	< 3.3	< 2.2	< 3.7

"gain" layer) is implanted under the n-type cathode. Application of a reverse bias voltage creates an intense electric field in this region of the sensor to start an avalanche multiplication for the electrons. The drift of the multiplied carriers through the thin substrate generates a fast signal with a time resolution of ~20–30 ps.

TOF layers were placed in each section of the ECCE detector and their positions were optimized to best compliment the Cherenkov detectors to cover the lowest possible particle momenta with a nearly 4π coverage, and maximize the time (25 ps) and position (pixel granularity of 0.5×2.6 mm^2) resolution. We further plan to use the DIRC timing measurement to supplement the AC-LGAD TOF measurement. This is especially useful for the $\eta \approx -1.5$ region where a gap exists in the AC-LGAD coverage and the DIRC offers excellent TOF resolution. Figure 17 (left) shows a visualization of the AC-LGAD geometry from the full GEANT4 simulation. Figure 17 (right) summarizes the performance of the TOF layers in each sector of the ECCE detector for π/K, e/π, and K/p separation.

The PID performance in terms of $1/\beta$ vs. p for the central barrel, as a benchmark, is shown in Fig. 18 (left) for an expected timing precision of 25 ps. The long dashed lines indicate the $\pm3\sigma$ range around mean $1/\beta$ values for each particle species. As shown, the $\pm3\sigma$ bands for pions and kaons are well separated over a momentum range of $0.1 < p < 1.3$ GeV/c, while proton identification is further extended to around 2.2 GeV/c. For electrons, clean separation from pions is achieved for $p <$ 0.45 GeV/c by at least 3σ. Similar performance studies have also been carried out for endcap TOFs.

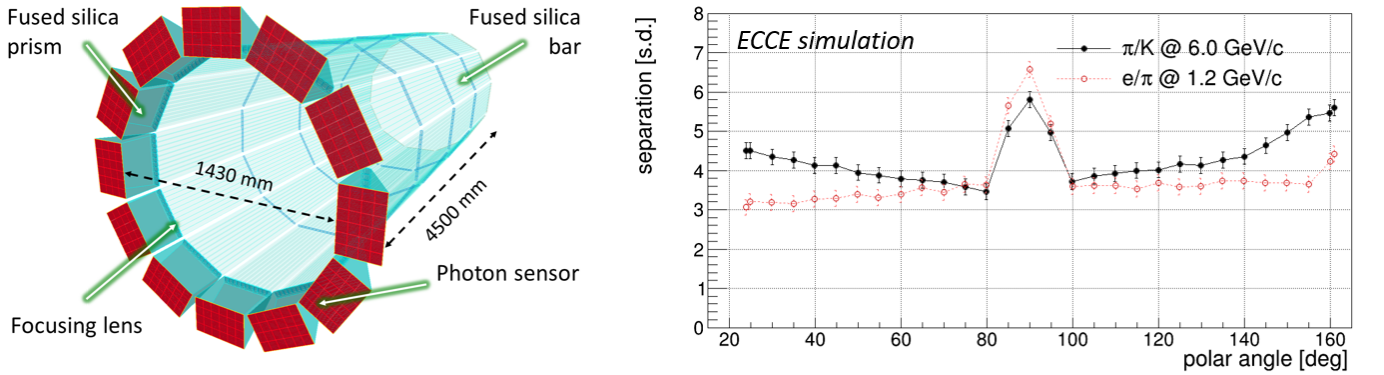

Figure 15: hpDIRC geometry (left) and expected PID performance (right) from the GEANT4 standalone simulation. The e/π and π/K separation power is shown in units of number of standard deviations as a function of the particle polar angle for e/π at 1.2 GeV/c and π/K up to 6 GeV/c.

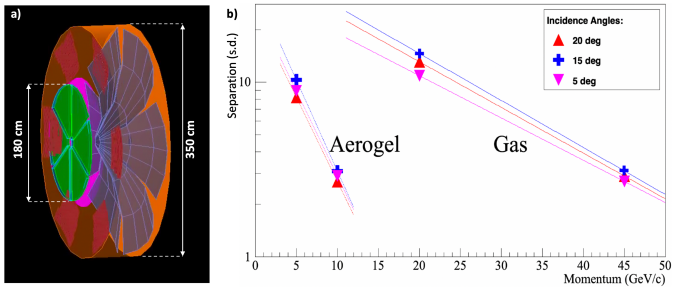

Figure 16: dRICH geometry (a) and expected performance (b) from the ECCE GEANT4 simulation. The K/π separation power is shown as a function of momentum for a simplified dRICH geometry (flat detector plane).

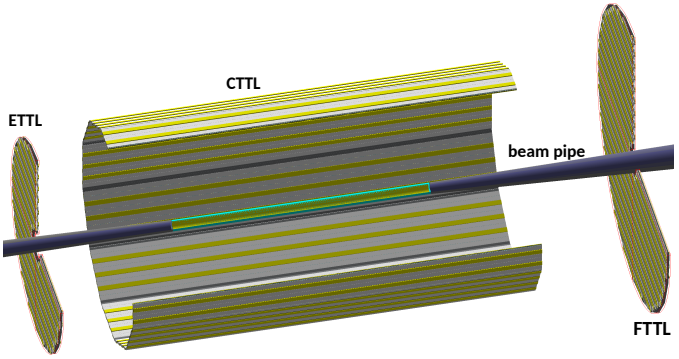

Figure 17: A schematic view of the timing and tracking layers (TTLs) in ECCE as simulated with GEANT4. The different subdetectors are called ETTL (electron endcap), CTTL (barrel) and FTTL (hadron endcap).

The resolution of the start time, t_0, is self-determined by the scattered electron and final-state hadrons via an iterative fitting procedure. The t_0 resolution was included in all performance studies and is shown in Fig. 18 (right). In addition to providing hadronic PID, the excellent position resolution of AC-LGADs TOF system significantly improves the momentum resolution of high momentum particles in the very forward region.

6. Electromagnetic and Hadronic Calorimetry

The ECCE electromagnetic calorimeter system[29] consists of three components which allow high precision electron detection and hadron suppression in the backward, barrel, and forward directions. Hadronic calorimetry is essential for the barrel and forward endcap regions for hadron and jet reconstruction performance. Jet yields in the backward region were found to be sufficiently infrequent that hadronic calorimetry would provide little to no scientific benefit. The details for all six calorimeters envisioned for ECCE can be found in Tab. 6.

6.1. Electron Endcap EM Calorimeter (EEMC)

The EEMC is a high-resolution electromagnetic calorimeter designed for precision measurements of the energy of scattered electrons and final-state photons in the electron-going region. The required energy resolution is driven by the need for a precise measurement of the scattered electron's energy and direction to determine the event kinematics in inclusive DIS events.

The design of the EEMC is based on an array of approximately 3000 lead tungsten crystals ($PbWO_4$) of size $2 \times 2 \times 20$ cm^3 ($\sim 22X_0$) and transverse size equal to its Moliere radius [34, 35] readout by SiPMs yielding an expected energy resolution of $2\%/\sqrt{E} + 1\%$, based on prototype beam test measurements by the EEEMCAL consortium and documented in the Yellow Report [2]. Fig. 20 shows the EEMC performance in the full ECCE detector simulations, consistent with the measurements. The corresponding particle identification power is shown in Fig. 21 for distinguishing electrons and pions (left) as well as separating the two photons from a neutral pion decay.

The choice of technology and overall design concept is common for all three proto-collaborations, with additional details of the development of this detector by the EEEMCal consortium summarized in the expression of interest [36]. The ECCE design only includes the $PbWO_4$ crystals due to the overall small detector radius. The EEEMCAL Consortium is planning to support one or more EIC detectors as needed and is therefore part of multiple detector proposals.

The EEMC is located inside the inner universal frame and al-

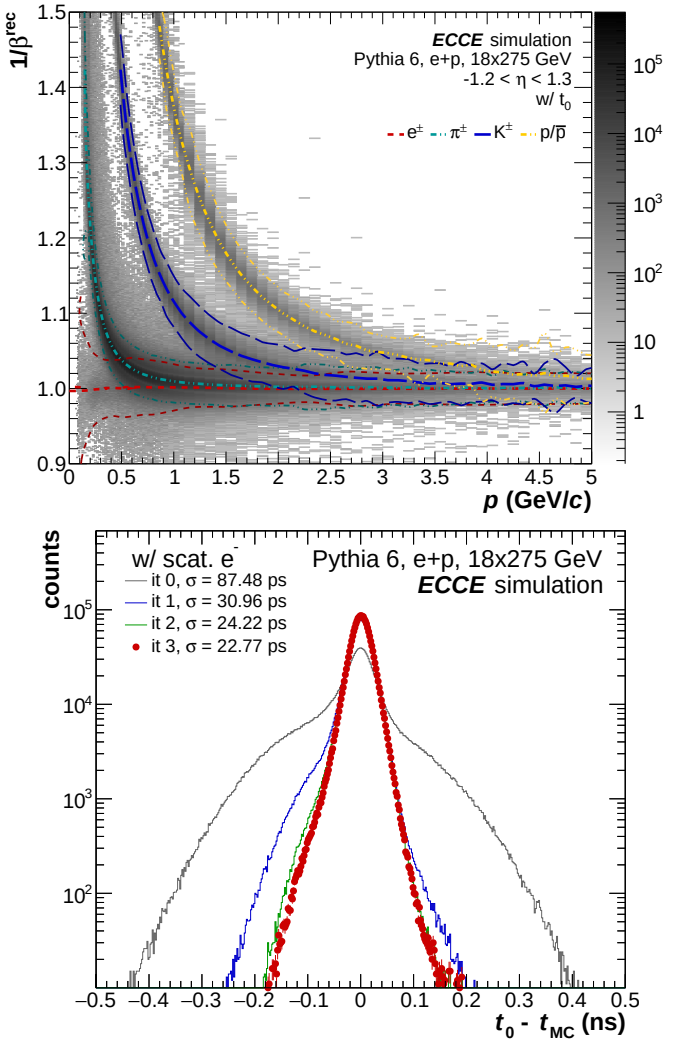

Figure 18: (left) Expected $1/\beta$ performance of the AC-LGADs TOF in the barrel as a function of particle momentum, assuming 25 ps time resolutions from full simulations including the start time estimates. (right) Expected start time (t_0) resolution as a function of iteration, for events where the scattered electron could be identified.

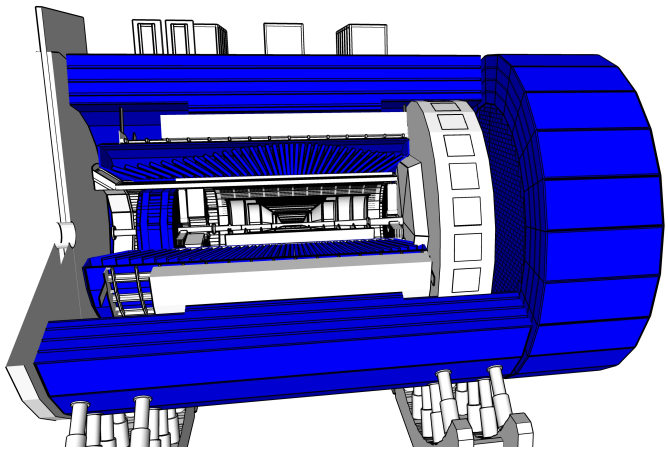

Figure 19: The electromagnetic and hadronic calorimeters in ECCE.

lows to reconstruct particles with $-3.4 < \eta < -1.8$. The lower η boundary is constrained by the proximity to the beam pipe and integration concerns with the beam pipe flange directly in front of the EEMC [37] in combination with the crystal dimensions. To extend the reach of the backward EEMC to a pseudorapidity of -3.7 one can envision a small inner calorimeter of 208 crystals and an outer calorimeter just behind it. There is sufficient longitudinal space accommodate this, but moving the outer calorimeter back could impact the acceptance in the transition region between the EEMC and the central barrel. If possible, this arrangement would allow the outer calorimeter to be removed over the beam pipe flange for maintenance, and separate removal of the small inner calorimeter in two halves. We intend to pursue this improvement to the baseline design as part of a detailed, integrated mechanical engineering design of the ECCE detector.

The EEEMCAL team has begun to organize activities into mechanical design, scintillator, readout, and software/simulation among the collaborating institutions. Design activities of the mechanical support structure commenced in 2021. The design is based on models of existing detectors that the team has recently constructed, in particular the Neutral Particle Spectrometer at Jefferson Lab [34]. As such, it is maturing rapidly and a document on mechanical design and integration has been completed [37].

6.2. Barrel EM Calorimeter (BEMC)

The barrel electromagnetic calorimeter (BEMC) is a projective homogeneous calorimeter based on an inorganic scintillator material that produces the shower due to high Z components. This allows for a cost-effective solution that provides excellent energy resolution and sufficient e/π rejection to achieve the EIC physics, which can be seen in Fig. 21. Further improvements are expected by determining exactly the Birk's constant and using shower shape criteria to distinguish elongated hadronic and rounder electromagnetic showers. The reference design of the BEMC is based on an array of approximately 9000 Scintillating Glass (SciGlass) blocks of size 4 x 4 x 45.5 cm^3, plus an additional 10cm of radial readout space. SciGlass has an expected energy resolution of $2.5\%/\sqrt{E} + 1.6\%$ based on earlier measurements [30, 31], comparable to $PbWO_4$ for a significantly lower cost. The energy resolution of the BEMC is shown in red in Fig. 20 (left) in its optimal acceptance ($-1.4 < \eta << 1.1$).

The development of SciGlass started with the generic detector R&D [38]. During this phase the team worked in close contact with producers of SciGlass to establish robust QA protocols at all stages of production to ensure the quality needed for the EIC. The validation of large-scale SciGlass production is now continued in the ongoing project R&D (eRD105). An initial 40 cm SciGlass bar of high quality has been produced this Fall (see Fig. 22 bottom right), and a prototype with nine 20-cm long SciGlass bars recently saw a successful beam test at Jefferson Lab, confirming the expected energy resolution. It is expected that multiple 45-cm long SciGlass bars will be produced in the next few months.

Just as for the EEMC, the BEMC attaches to the outer universal frame. Adapting the geometry of the homogeneous barrel

Table 6: Specifications and properties for the electromagnetic and hadronic calorimeters from the Geant simulation. Note that d_{act} does not include readout. The acceptance of the EEMC can be achieved with a small inner calorimeter as discussed in the text. The energy resolutions for EEMC, BEMC and OHCAL are those expected from prototype tests or experiments [2, 30, 31, 32]. Further details can be found in the [5].

	EEMC	BEMC	FEMC	IHCAL	OHCAL	LFHCAL
tower size	$2x2x20$ cm^3	$4x4x45.5$ cm^3 projective	in: $1x1x37.5$ cm^3 out: $1.6x1.6x37.5$ cm^3 projective	$\Delta\eta \sim 0.1$ $\Delta\varphi \sim 0.1$ $l \sim 4.5$ cm	$\Delta\eta \sim 0.1$ $\Delta\varphi \sim 0.1$ $l \sim 88$ cm	$5x5x140$ cm^3
material	$PbWO_4$	SciGlass	Pb/Scintillator	Steel/ Scintillator	Steel/ Scintillator	Steel/W/ Scintillator
d_{abs}	-	-	1.6 mm	13 mm	in: 10.2 mm out: 14.7 mm	16 mm
d_{act}	20 cm	45.5 cm	4 mm	7 mm	7 mm	4 mm
N_{layers}	1	1	66	4	5	70
$N_{towers(channel)}$	2876	8960	19200/34416	1728	1536	9040(63280)
X/X_O	~ 20	~ 16	~ 19	~ 2	$36-48$	$65-72$
R_M	2.73 cm	3.58 cm	5.18 cm	2.48 cm	14.40 cm	21.11cm
f_{sampl}	0.914	0.970	0.220	0.059	0.035	0.040
λ/λ_0	~ 0.9	~ 1.6	~ 0.9	~ 0.2	$\sim 4-5$	$7.6-8.2$
η acceptance	$-3.7 < \eta < -1.8$	$-1.7 < \eta < 1.3$	$1.3 < \eta < 4$	$1.1 < \eta < 1.1$	$1.1 < \eta < 1.1$	$1.1 < \eta < 4$
resolution						
- energy	$2/\sqrt{E} \oplus 1$	$2.5/\sqrt{E} \oplus 1.6$	$7.1/\sqrt{E} \oplus 0.3$		$75/\sqrt{E} \oplus 14.5$	$33.2/\sqrt{E} \oplus 1.4$
- φ	~ 0.03	~ 0.05	~ 0.04		~ 0.1	~ 0.25
- η	~ 0.015	~ 0.018	~ 0.02		~ 0.06	~ 0.08

EM calorimeter at PANDA [39], the BEMC towers are organized in 128 blocks by ϕ slice and 70 blocks in η, which will be assembled in super modules stretching the full length in η and 8 towers in φ for installation in the universal frame. Figure 22 (top) shows a sketch of the BEMC illustrating the at least six different families of glass blocks needed to achieve the required projectivity in η. For comparison, PANDA uses 11 different crystal types for their barrel. The optimal number of families still has to be determined, optimizing for efficient production as well as minimal leakage between towers. Also indicated is a schematic of the support box (modeled after the PANDA barrel calorimeter) for readout and other services that mounts to the outer universal frame.

The BEMC has been designed with projectivity in η and ϕ. This requires that the tower angular deflection depends on its location in the calorimeter. Additionally, the towers have a stronger inclination at higher absolute pseudorapidities, leading to an asymmetric tapered shape of the glass blocks, which increases with $|\eta|$. Their front face is tilted such that it is facing the interaction point shifted by $z = -10$ cm and tilted 10° in the azimuthal direction, to avoid channeling between the towers. Such a projective design delivers a more uniform performance, mainly aimed at the transition regions between the barrel and forward and backward regions, as defined by the length to bore ratio of the magnet. All the towers have the same length, 45.5 cm (not including $\sim$ 10cm readout), and inner size 4 x 4 cm in the present simulation. However, the upper area sections vary from 5 to 6.6 cm in each side depending on their location.

6.3. Barrel Hadron Calorimeters: OHCAL and IHCAL

The energy resolution of reconstructed jets in the central barrel will be dominated by the track momentum resolution, as the jets in this region are relatively low momentum and the measurement of the energy in the hadronic calorimeter does not improve knowledge of the track momentum. For jet reconstruction, the primary use for a hadronic calorimeter in the central barrel will be to collect neutral hadronic energy and thus improve the overall knowledge of the Jet Energy Scale (JES). For this purpose, the Yellow Report indicates that a resolution of $(80-100)\%/\sqrt{E} \oplus (7-10)\%$ will be adequate. Therefore, we decided to reuse the sPHENIX Outer Hadronic Calorimeter (OHCAL), which instruments the barrel flux return steel of the BaBar solenoid to provide hadronic calorimetery with an energy resolution of $75\%/\sqrt{E} \oplus 14.5\%$, as measured in test beam. We also plan to instrument the support for the barrel electromagnetic calorimeter to provide an additional longitudinal segment of hadronic calorimetry. This will provide an Inner Hadronic Calorimeter (IHCAL) very similar in design to the sPHENIX inner HCAL. The inner HCAL is useful to monitor shower leakage from the barrel electromagnetic calorimeter as well as improve the calibration of the combined calorimeter system.

The basic calorimeter concept for the IHCAL/OHCAL is a sampling calorimeter with absorber plates tilted from the radial direction. This design provides more uniform sampling in azimuth and gives some information about the longitudinal shower development. The outer HCAL uses tapered 1020 magnet steel plates which maintain a uniform gap size for the scintillating tiles. The inner HCAL will be made from stainless steel or aluminium as it sits inside the magnetic field. The Inner HCAL will not require tapered plates as studies have shown that taperig the shorter inner HCAL plates is not necessary, and tapering them substantially increases the machining cost. Extruded tiles of plastic scintillator with an embedded wavelength shifting fiber are interspersed between the absorber plates and read out at the outer radius with silicon photomultipliers (SiPMs). A 12 degree tilt angle relative to the radius is chosen in the outer HCAL so that a radial track from the center of the interaction region traverses at least four scintillator tiles. The inner HCAL is tilted at 36 degrees, in the opposite direc-

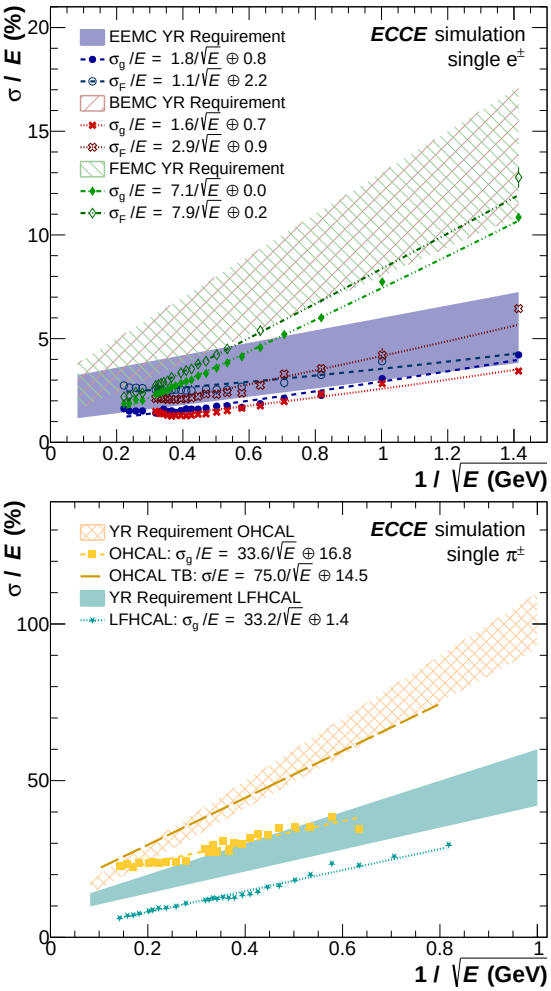

Figure 20: The electron (top) and pion (bottom) energy resolution of the electromagnetic and hadronic calorimeters, respectively, compared to the Yellow Report requirement (shaded/hashed area). The data points and fits indicated as σ_g/E are based on the Gaussian width of the resolution peaks, while σ_F/E is based on the FWHM. The energy resolution based on a test beam for the OHCAL is shown for comparison [33].

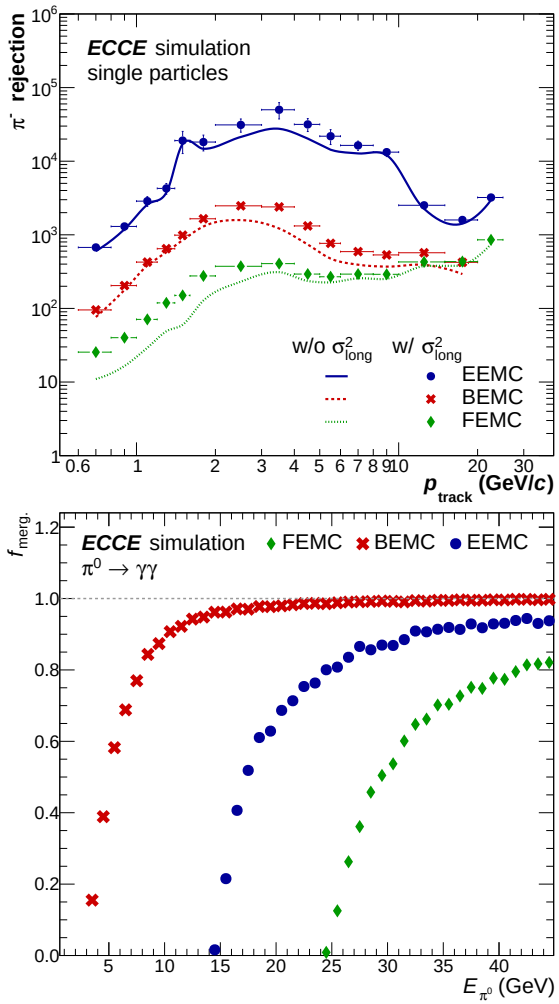

Figure 21: (top) Pion rejection factor for the different ECals with $E/p > 1 - 1.6\sigma_E/E$ and shower shape cuts applied as a function of true and reconstructed momentum. (bottom) Fraction of neutral pions for which the showers from their decay photons are merged into a single cluster and can not be reconstructed using an invariant-mass-based approach for the different electromagnetic calorimeters.

tion compared to the outer HCAL. Each tile has a single SiPM, and the analog signal from each tile in a tower (five for the OHCAL, four for the IHCAL) are ganged to a single preamplifier channel to form a calorimeter tower. Tiles are divided in slices of pseudorapidity so that the overall segmentation is $\Delta\eta\times\Delta\phi \sim 0.1\times0.1$. The Outer HCal is longitudinally symmetric around the interaction point and requires 24 tiles along the η direction. The design thus requires 12 different shapes for tiles for each longitudinal segment. The inner HCAL is extended along the backwards direction, and is comprised of 12 tiles in the forward η direction and 15 tiles in the backward η direction. There are 1536 readout channels (towers) in the OHCAL and 1728 channels for the IHCAL.

6.4. Hadron Endcap Electromagnetic (FEMC) and Hadronic Calorimeter (LFHCAL)

The desired performance in the forward region is governed by the jet energy resolution requirements, as well as very good energy resolution ($35\%/\sqrt{E}$ to reach the desired resolution in δx) for the physics processes connected to the origin of mass. Additionally, an excellent position resolution in particular within the ECal is required for PID within the jet. Within this region a higher particle density is expected than in the central barrel, supporting the need for excellent position an energy resolution in both calorimeters. Both detector systems need to be able to handle the expected energies of incoming particles up to 150 GeV. Due to the asymmetric collision system, these calorimeters are therefore focused strongly on high energetic particle shower containment while still providing good energy resolution at low energies.

We envision the forward calorimeter system as an integrated ECal and HCal, where the installation units, where appropriate, are constructed in a common casing. These so-called modules will consist of an electro-magnetic calorimeter segment in the front which is part of the forward EMCal (FEMC) followed by a hadronic calorimeter segment which is part of the longitudi-

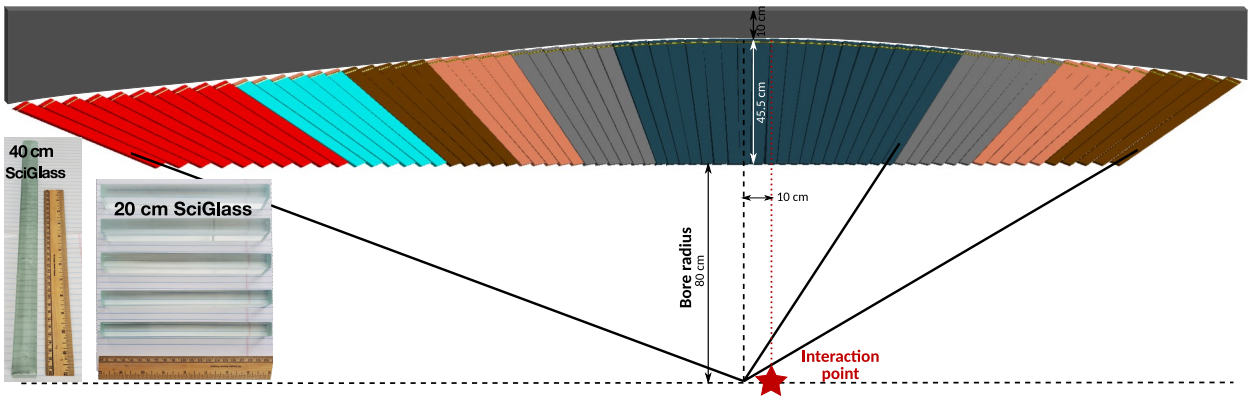

Figure 22: Side cut view of the barrel assembly from Geant4 illustrating the six different families of glass block sizes needed to achieve the needed projectivity. Also shown is a schematic of the support box (grey) based on the PANDA design that holds readout, cooling, and other services and mounts to the outer universal frame.

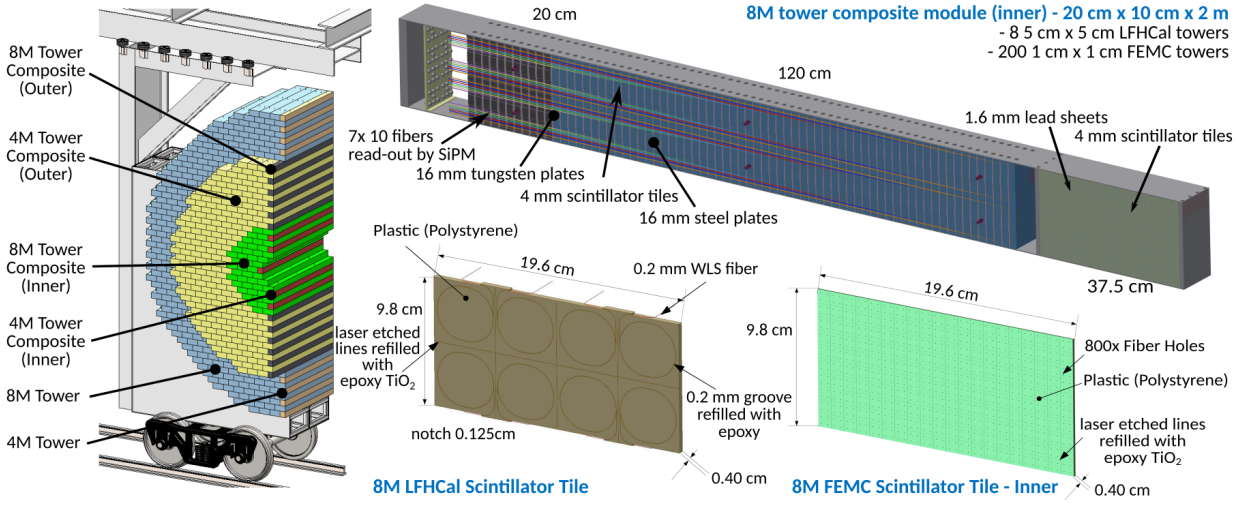

Figure 23: Details of the combined FEMC and LFHCal design, indicating a fully assembled half disk, the 8-tower module design and the individual scintillator tile designs for the an LFHCAL-FEMC 8M tower inner module.

nally separated HCal (LFHCal). In between these segments a read-out section is foreseen for the ECal. The modules of up to four different sizes will be installed in half shells surrounding the beam pipe, which are movable on steel trolleys to give access to the inner detectors in the barrel in the hadron going direction. This integrated E- and HCal design reduces the dead material in the detector acceptance and allows for an easier installation in the experimental hall.

The forward ECal (FEMC) will be a Pb-Scintillator shashlik calorimeter. It is placed after the tracking and particle identification detectors and made up of two half disks with a radius of about 1.83m. The calorimeter is based on the lead-scintillator "shashlik" calorimeter designs already utilized for ALICE, STAR and PHENIX. However, it employs more modern techniques for the readout as well as scintillation tile separation. The towers were designed to be smaller than the Moliere-radius in order to allow for a further shower separation at high rapidity.

The towers have an active depth of 37.5 cm with and consist out of 66 layer of 0.16 cm Pb sheets and 0.4 cm scintillator material, as can be seen in Tab. 6. Due to the high occupancy of the detector at large pseudorapities and the collimation of the particles in this area in physical space, the tower size will vary depending on its radial position with respect to the beam axis. Towers which are close to the beam pipe ($R < 0.8$ m) will have a active tower size of 1 cm×1 cm×37.5 cm. For the outer radii this granularity is not necessary and thus the size is increased to 1.65 cm×1.65 cm×37.5 cm. In order to collect the light produced in the scintillator tiles, each scintillator and Pb-plate is pierced by four 0.2 mm-wavelength shifting fibers. These fibers are used to collect the light generated in the scintillators across all 66 layers. All four fibers are read out together by one silicon photomultiplier (SiPM). The FEMC is constructed with modules size of at least 5 cm×5 cm×37.5 cm (1M module) up to 10 cm×20 cm×37.5 cm (8M modules) aligning with the module sizes of the hadronic calorimeter. In order to separate the light produced in different segments of the 8M-tile a gap between the 1 cm×1 cm tower tiles is created by edging into the scintillator using a laser. These 0.37 mm deep gaps are then refilled with a mixture of epoxy and titanium-oxide in order to

reduce the light cross talk among different towers. Depending on their radial position this leads to either 72 or 200 read-out towers in one 8M modules.

The longitudinally segmented forward HCal (LFHCAL) is a Steel-Tungsten-Scintillator calorimeter adapted from the PSD calorimeter for the NA61/SHINE experiment [40], but it has been severely modified to meet the desired physics performance laid out in the Yellow Report. It is made up of two half disks with a radius of about 2.6 m.

The LFHCAL towers have an active depth of 1.4 m with an additional space for the readout of about 20–30 cm depending on their radial position, as seen in Table 6. Each tower consists out of 70 layers of 1.6 cm absorber and 0.4 cm scintillator material. For the first 60 layers the absorber material is steel, while the last 10 layers serve as tail catcher and are thus made out of tungsten to maximize the interaction length within the available space. The front face of the tower is 5 cm×5 cm.

In each scintillator a loop of wavelength shifting fiber is embedded, as can be seen in Fig. 23 (middle). Ten consecutive fibers in a tower are read out together by one Silicon photo multiplier, leading to seven samples per tower. The towers are constructed in units of 8-,4-, 2- and 1-tower modules to ease the construction and reduce the dead space between the towers and the active detection area. Similar as for the FEMC the scintillator tiles in the larger modules are made out of one piece and then separated by a gaps refilled with epoxy and titanium oxide to reduce light cross-talk among the different readout towers. For the same purpose the wavelength shifting fibers running on the sides of the towers are grouped early on according to their readout unit and separated by thin plastic pieces over the full length. They terminate in one common light collector which is directly attached to a SiPM. The entire detector will consist of 63280 readout channels grouped in 9040 read-out towers.

The majority of the calorimeter will be built out of 8-tower modules (∼1091) which are stacked in the support frame using a lego-like system for alignment and internal stability, as can be seen in Fig. 23 (left). The remaining module sizes are necessary to fill the gaps at the edges and around the beam pipe to allow for maximum coverage. The absorber plates in the modules are held to their frame by four screws each. To leave space for the read-out fibers, the steel and scintillator plates are not entirely square but equipped with 1.25 mm grooves, creating the fiber channels on the sides. These fiber channels are covered by 0.5 mm thin steel plates for protection after module installation and testing, in order to protect the fragile fibers. For internal alignment we rely on the usage of 1–2 cm steel pins in the LFHCal part which are directly anchored to the steel or tungsten absorber plates. Afterwards the modules will be self-supporting within the outer support frame. The steel in the LFHCAL serves as flux return for the BaBar magnet, thus a significant force is exerted on the calorimeter, which needs to be compensated for by the frame and internal support structure. The achieved energy resolution accoding to the simulations for both calorimeters can be found in Fig. 20. The required resolutions can be met in both cases and further improvements can be expected using machine learning for the clusterization which proves challenging in this direction. The excellent position resolution in the FEMC should in addition allow the effective separation of electrons and pions as well neutral pion decays, as seen in Fig. 21.

7. Far-Forward/Far-Backward Detectors

A schematic of the far-forward detectors is shown in Figure 24 and include the B0 spectrometer, off-momentum trackers, Roman Pots and ZDC (see Table 7 for position and dimensions). The far-backward region consists of two detector systems (low-Q^2 tagger and luminosity monitor). All far-forward/far-backward detectors are required for the EIC physics as described in the Yellow Report. The following describes their setup and performance. For further details, see Ref. [41].

7.1. B0 Detector

The B0 spectrometer is located inside B0pf dipole magnet. Its main use is to measure forward going hadrons and photons for exclusive reactions. The B0 acceptance is defined by the B0pf magnet. Its design is challenging due to the two beam pipes (electron and hadron) that it needs to accommodate and the fact that they are not parallel to each other due to the 0.025 mrad IP6 crossing angle. Moreover, the service access to the detectors inside of the dipole is only possible from the IP side, where the distance between the beam pipes is narrowest. Following these limitations the B0 detector require using compact and efficient detection technologies.

Our design uses four AC-LGAD tracker layers with 30 cm spacing between each layer. They will provide charged particle detection for $6 < \theta < 22.5$ mrad. The use of AC-LGAD sensors will allow good position and timing resolutions. The AC-LGAD sensor will have a 3.2x3.2 cm^2 area, with four dedicated ASIC units on each sensor. In addition, a $PbWO_4$ calorimeter will be positioned behind the fourth tracking layer at 683 cm from the IP. Using the $PbWO_4$ in the B0 calorimeter will increase the detection fraction of the two decayed γs from the u-Channel π_0 production from 40% to 100%, and enable measurements of u-Channel DVCS events which without it will be swamped by the π^0 events with single γ detected. The calorimeter is constructed from 10 cm long 2x2 cm^2 $PbWO_4$ crystals and positioned to leave 7 cm for the readout system. Both trackers and Calorimeter has oval holes in the center to accommodate the hadron beam pipe, and a cutaway in the side to accommodate the electron beam and allow installation and service of the detector system (see Fig. 24).

Figure 25 (left) shows the simulated momentum and its resolution $\sigma[\Delta p/p]$ as a function of truth momentum. It is below 5% for the studied kinematic region. The effect of the presence of dead material (2mm of Cu after each Si plane) layers on the momentum resolution is also shown and estimated to degrade the resolution by 2% uniformly as a function of p. The photon energy reconstructed in the B0 calorimeter and its resolution are shown in Fig 25 (right) for photons originating in the interaction vertex with pseudorapidity $4 < \eta < 6$ and energy $0 < E_\gamma < 60$ GeV. It is found to be below 7% for the studied

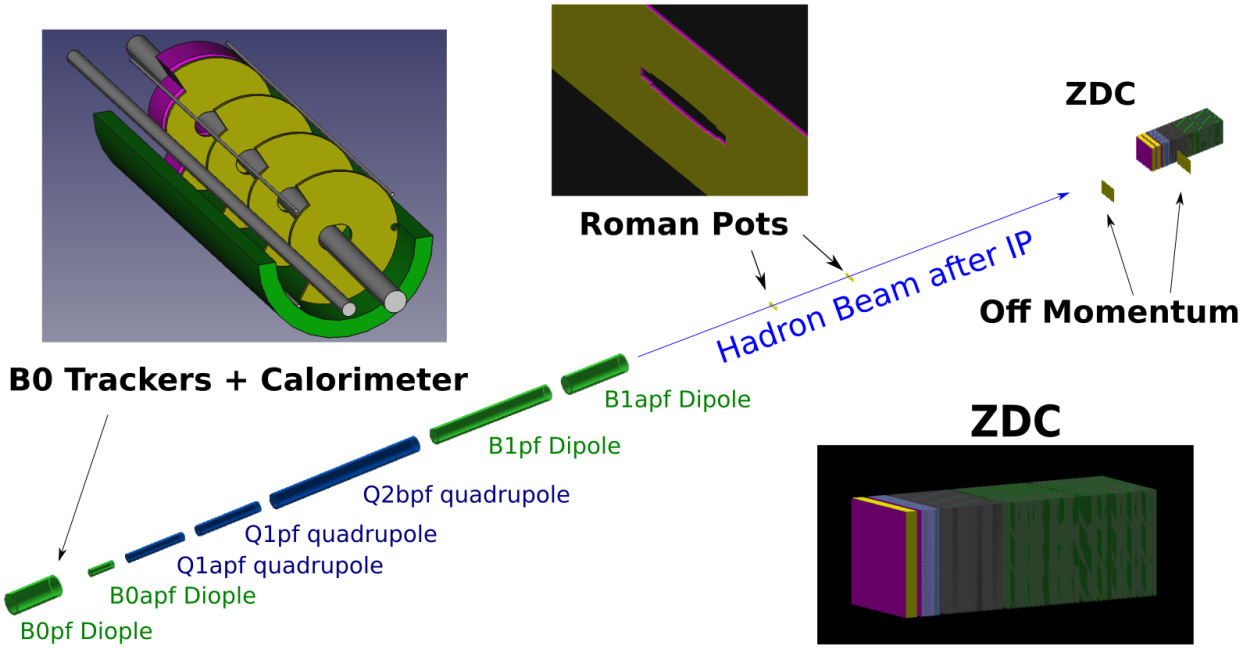

Figure 24: The layout of the EIC Far-Forward region.

Table 7: Summary of far-forward detector locations and angular acceptances for charged hadrons, neutrons, photons, and light nuclei or nuclear fragments. In some cases, the angular acceptance is not uniform in ϕ, as noted in the table. For the three silicon detectors (Roman Pots, Off-Momentum Detectors, and B0 spectrometer) a depth is not given, just the 2D size of the silicon plane. For the Roman Pots and Off-Momentum Detectors, the simulations have two silicon planes spaced 2m apart, while the B0 detectors have four silicon planes evenly spaced along the first 1.0 m length of the B0pf dipole magnet bore. The planes have a "hole" for the passage of the hadron beam pipe that has a radius of 3.2 cm.

Detector	**(x,z) Position [m]**	**Dimensions**	θ **[mrad]**	**Notes**
ZDC	(-0.96, 37.5)	(60cm, 60cm, 1.62m)	$\theta < 5.5$	~4.0 mrad at $\phi = \pi$
Roman Pots (2 stations)	(-0.83, 26.0) (-0.92, 28.0)	(30cm, 10cm)	$0.0 < \theta < 5.5$	$10\,\sigma$ cut.
Off-Momentum Detector	(-1.62, 34.5), (-1.71, 36.5)	(50cm, 35cm)	$0.0 < \theta < 5.0$	$0.4 < x_L < 0.6$
B0 Trackers and Calorimeter	(x = -0.15, 5.8 < z < 7.0)	(32cm, 38m)	$6.0 < \theta < 22.5$	~20 mrad at ϕ=0

kinematic region. In general about 60% of the energy is reconstructed within a 2x2 crystal grid with some dips in efficiency at low E_γ and high η.

7.2. Roman Pots

Diffractive processes such as deeply virtual Compton scattering will produce protons with high energy and small p_T with only a small separation from the hadron beam. The Roman Pots are designed to detect such particles. They will consist of two double-layer 25x12 cm^2 AC-LGAD stations, located inside the beam line 26 and 28 m downstream the interaction point and 10σ from the main beam. This technology will provide the necessary position and timing resolution for a precise measurement with minimized background.

The vacuum environment will require special cooling. We will use heat sinks made of metal foam through which compressed air will flow. Such cooling systems are already in use at the LHC.

7.3. Off-momentum Detectors

Off-momentum detectors complement the Roman Pots by measuring charged particles that have a smaller magnetic rigidity than the main hadron beam. Such particles will be bent outside the beam pipe. The detectors consist of tracking planes based on AC-LGAD sensors.

Good timing resolution on the order of 10 ns facilitates the rejection of pileup and beam related background, since particles that do not come directly from the interaction point will have a different flight path than the particles of interest. Such techniques have been used extensively by the CMS Precision Proton Spectrometer and the ATLAS Forward Proton Group at the LHC.

7.4. Zero Degree Calorimeter (ZDC)

The size of the ECCE ZDC is 60 cm×60 cm×162 cm, and the weight is greater than 6t. As shown in Fig. 24, the ZDC consists of $PbWO_4$ crystal layer, W/Si layer, Pb/Si layer and Pb/Scintillator layer.

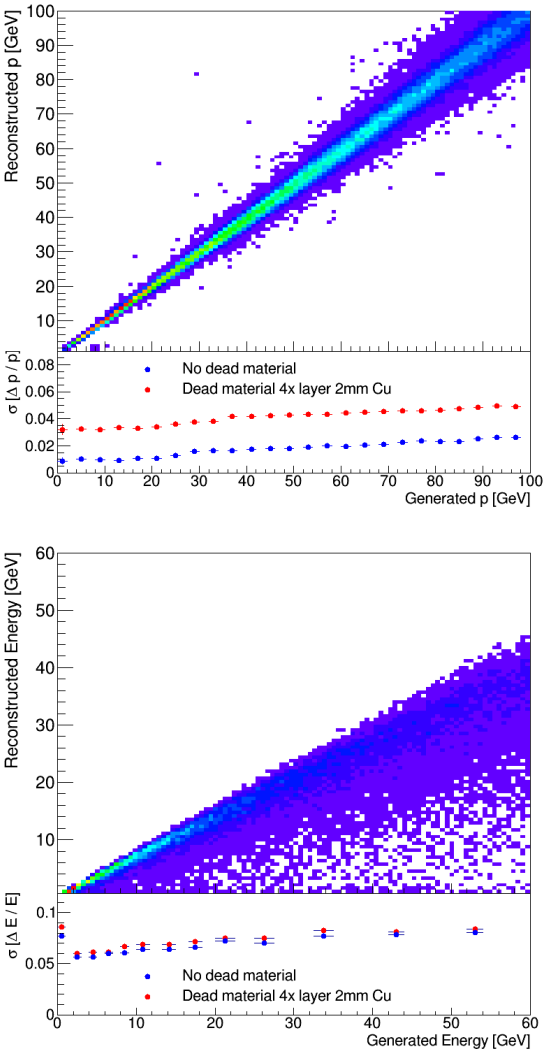

Figure 25: (top) Reconstructed momentum and its resolution for μ^- tracks found in the B0 tracker; (bottom) reconstructed energy of photons and its resolution in the B0 calorimeter.

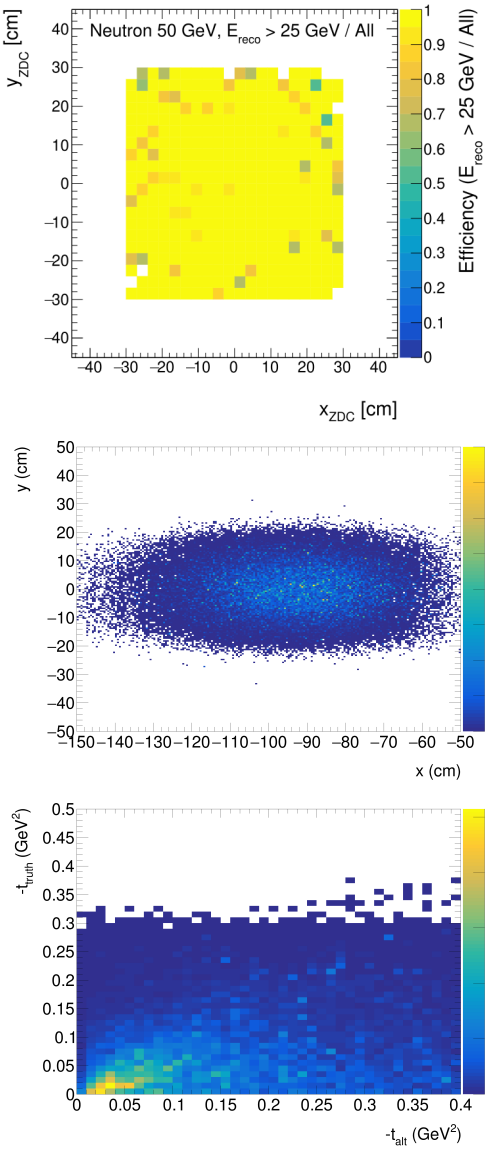

Figure 26: (top) ZDC detection efficiency for neutrons in its local coordinate system. (middle) Detection distribution of neutron hits in the ZDC for meson structure function processes without the beam pipe blocking contribution. z-axis reflects the normalized yield. (bottom) Reconstructed t versus true t, where t is reconstructed as from the baryon information, $t_{alt} = (p_p - p_n)^2$, which is reliable with a resolution of < 0.025 GeV^2.

The estimated energy resolution for high energy photons is well below the required value. For the low energy photons, estimated resolution for 100 MeV photons using 5% smearing reaches 20%, which is is still acceptable. The neutron energy resolution is consistent with and even smaller than the Yellow Report required value of $50\%/\sqrt{E} + 5\%$. For 40 GeV and 20 GeV photons, the position resolution is estimated as 1.1 mm and 1.5 mm respectively. On the crystal layer, the cluster finding efficiency is $> 95\%$ for both 20 GeV photons and 100 MeV photons with the seed energy requirement of 15 MeV for the clustering.

While the ZDC is used for a variety of measurements in ECCE, we evaluate its performance here using simulations of meson structure function measurements that represent a key performance driver for this detector. In these reactions, neutrons from the Sullivan process carry 80-98% of the proton beam momentum and are detected at far-forward angles in the ZDC. The detection fraction for neutrons (t resolution) is 59% (0.019 GeV^2) at the lowest, 5 on 41, and 100% (0.005-0.007 GeV^2) at the higher energy combinations. Due to the large size and high inherent ZDC detection efficiency (Fig. 26 (left)), the ECCE detection efficiency for these events is quite high, $\sim 80\%$, and nearly independent of Q^2. A density plot of event distribution is shown in the left panel of Fig. 26. The detection efficiency is highest for events with small $-t < 0.15$ GeV^2, which are needed for measurements such as the pion form factor, and decreases rapidly with $-t$. The t-range of optimal acceptance is dictated by the size of the ZDC, as the energetic neutrons from higher $-t$ events are emitted at an angle larger than the ZDC acceptance.

We further find the ZDC to offer excellent reconstruction of t. Compared with the t reconstruction from the measurement of the π^+ and e' tracks, the ZDC's baryon measurement is significantly more reliable, in agreement with EIC YR studies. Due to the excellent position resolution of the ZDC, the neutron track momentum is reconstructed to within 1% of the "true" momentum.With this information, t is reconstructed from the neutron track in a manner that reproduces the true value very closely, see Fig. 26 (right). Such a reliable reconstruction of t is essential for many processes such as the pion form factor measurement, where the rapid fall off of the cross section needs to be measured to confirm the dominance of the Sullivan mechanism. The high quality ZDC proposed by ECCE is clearly of paramount importance to the feasibility of such measurements.

7.5. Low-Q^2 Tagger

The low Q^2-tagger will facilitate measurement of reactions with small cross sections, e.g. timelike Compton scattering. Measuring the scatted electron will allow the s dependence to be measured as well as giving some measure of the production four momentum transfer, or t. When coupled with proton detection in the far forward region there will be the possibility of applying exclusivity cuts.

The low-Q^2 Tagger consists of two stations, located 24 m and 37 m from the interaction point. Each station includes a double layered AC-LGAD tracker, followed by a $PbWO_4$ electromagnetic calorimeter. The detectors surface areas are 40.5 cm×40.5 cm at 24 m and 30 cm×21 cm at 37 m and their calorimeters both use 20 cm long 2 cm×2 cm $PbWO_4$ crystals.

The tracking planes enable the determination of the electron scattering angle, that in turn facilitate a precise determination of Q^2. The calorimeter provides an energy measurement to complement the tracking and provide additional shower shape information to confirm that the particle really is an electron.

7.6. Luminosity Monitors

For the luminosity measurements, an accuracy of the order of 1% is required, or relative luminosity determination exceeding 10^{-4} precision. The latter is driven by the size of the asymmetries we want to measure. This requirement drives the utilization of several complementary approaches for both relative and absolute measurements of the luminosity, allowing us to understand and constrain the beam-size effects, synchrotron radiation, as well as systematic uncertainties. The approach we will follow is based on existing experience from HERA. The absolute luminosity is determined by correlating the total energy in the calorimeter with the number of photons. The low-Q^2 tagger can also provide key information on the relative luminosities and thus impose further constraints on the luminosity determination.

The luminosity monitor will be located along the photon zero-degree line in the far backward region and will measure bremsstrahlung photons. It uses both a dedicated calorimeter to measure direct photons, and two spectrometer arms to measure e^+e^- pairs from conversions. The direct photon calorimeter will have a size of 16 cm×16 cm and will use 20cm long 2x2 cm^2 $PbWO_4$ crystals. The e^+ and e^- from photon conversions will be deflected above and below the main photon beam by a small dipole magnet before entering the spectrometer arms. Each arm includes two 8×16 cm^2 AC-LGAD tracking layers followed by a $PbWO_4$ calorimeter with a matching surface area (also made of 20cm long 2x2 cm^2 crystals). The tracking planes in the e^+/e^- arms will allow reconstructing the gamma spot to help understand and constraint beam-size effects.

8. Electronics and Data Acquisition

The general design of the ECCE data acquisition builds on the sPHENIX DAQ system and many of the JLAB streaming readout systems under test [41]. These systems already incorporate and demonstrate almost all concepts of the envisioned ECCE DAQ system. The ECCE DAQ system will be built around a trigger-less Streaming Readout (SRO) concept from the start.

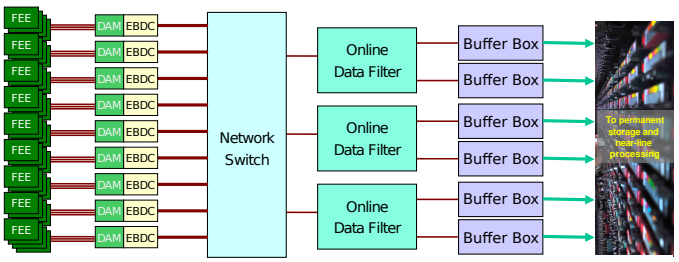

Figure 27: The schematic view of the ECCE Data Acquisition system. With the detector systems connecting to FEE cards from the left, the digitized data are sent to "Data Aggregation Modules" (DAM) that filter and package the data. The "Event Buffer and Data Compressor" (EBDC) nodes perform another filter, noise suppression, and clustering step on the scope of the connected detector channels, and align the hits by timing value. The data are then sent to processing nodes that perform a filtering/triggering step on the entire detector view. Data from selected crossings then get stored temporarily on large file servers ("Buffer Boxes") before being sent to long-term storage at the computing center.

As detailed in the Yellow Report [2], the Streaming Readout concept has proven superior to a classic triggered scheme in several ways. Modern readout technologies often do not follow a strict "event" paradigm in the sense that data from collider crossing n are already arriving from one front-end, while other parts can still be transmitting data from trigger n-1, n-2, or earlier crossings. In streaming mode, there is no need to wait for the completion of the data transmission from a given crossing, as the data parts are later re-assembled by their embedded clock information. This usually leads to a higher data throughput when compared to a triggered mode.

The other advantage is that classic trigger setups are always limited in their selection power because the amount of data they can sample to arrive at a trigger decision is generally much more restricted than in streaming mode, where the software- or firmware-based selection algorithms have, at least in principle, access to the data from all detector components. The processing power to increase the quality of the event selection has become cheaper every year, and this trend is expected to continue.

Table 8: PID Detector ASICs and channel counts. The ASICs for the time-of-flight detectors are currently under development in eRD112

Detector	ASIC	Channels
hpDIRC	High Density SoC	69,632
CTTL	eRD112	8.6M
mRICH	High Density SoC	65.5K
ETTL	eRD112	0.92M
dRICH	MAROC3	5.4K
FTTL	eRD112	1.84M
Roman Pots	eRD112	524.3K
B0 Detector	eRD112	2.6M
Off-Momentum Detectors	eRD112	1.8M
Low-Q^2 Tagger	eRD112	4.6M
Luminosity Monitor	eRD112	268.4K

In a trigger-less data acquisition scheme, each channel with a signal exceeding a threshold is transferred after being labeled with a time-stamp, irregardless of the status of the other channels. The resulting data is often a waveform, or a list of fired pixel-type detector elements, or some combination of both. Subsequent processing layers reduce the amount of information by categorizing the information by time, so that eventually the detector information of one bunch crossing is together in one place. While traversing the various processing layers, data get filtered and packaged, and waveform processing and clustering algorithms are applied that further reduce the amount of data to a few key properties.

The progression of processing layers is schematically shown in Fig. 27. With the connections from the detector, typically fibers, coming from the left, detector-specific Front-End Electronics (FEE) cards digitize the signals, and send digital data on to the "Data Aggregation Module" (DAM). An current example of such a DAM is the ATLAS FELIX card [15].

The DAM plays a central role as it provides a common detector interface for the expected large variety of detector readout technologies that are found upstream of the DAM. While the DAM still needs to run detector-specific firmware to receive and package the data, it provides common hardware and common APIs for the subsequent data handling, and greatly reduces the software development efforts.

The "Event Buffer and Data Compressor" (EBDC) nodes, the offline data filter, and the file servers ("Buffer Boxes") shown in Fig 27 are Linux PCs that form the next layers of the processing chain.

The Front End Electronics including ASICs will need to be compatible with the streaming readout DAQ system plan. FEE will need to support continuous sampling modes and not require an external trigger to convert detector signals because this will introduce large unwanted DAQ deadtime. Full waveform sampling for high occupancy detectors with zero suppression and feature extraction (time & charge) will be needed for a flexible streaming readout system.

ASIC devices have been carefully evaluated for each of the ECCE experiment detector systems and are listed for the PID detectors in Table 8. High channel counts for the hpDIRC and mRICH detectors have based their readout on the High Density System-on-a-Chip (HDSoC) ASIC that is commercially produced by Nalu Scientific. The HDSoC has 64 channels and a very high bandwidth sampling ADC for waveform capture and feature extraction modes. This ASIC will support the streaming readout model. The dRICH detector is planning to use the MAROC3 ASIC which is a 64-channel device that interfaces directly to a 64 pixel maPMT device. Supporting electronics to configure the MAROC3 and provide streaming data has been in use at Jefferson Lab for the CLAS12 RICH detector for several years and is a mature technology and the MAROC3 device is now commercially available. The 64-channel SAMPA amplifier and digitizer ASIC is strongly considered for the μRWELL tracking detectors and is a very good example of an ASIC that will operate within the requirements of a streaming readout front end.

AC-Low Gain Avalanche Diodes (AC-LGAD) sensors planned for the Time-Of-Flight PID detector system, where the channel counts are very dense, as well as the far-forward detectors. Development of front-end electronics, particularly ASIC chips, for AC-LGAD readout is part of the eRD112 project for targeted EIC detector R&D. The strategy is to base designs on the ATLAS ALTIROC (130 nm) and CMS ETROC (65 nm) designs as a starting point, and reduce the pixel granularity and timing jitter to meet the EIC requirements. Specifically, the IJCLab (Orsay)/ OMEGA (IN2P3-École Polytechnique) group on the eRD112 team is a main developer of the ATLAS ALTIROC, and will play the lead role at the initial stage of ASIC development. A preliminary 130 nm ASIC design with a pitch size of 0.5 mm×0.5 mm has been achieved as a stepping stone, that meets the requirements set by the EIC Roman Pot, B0 detector, and Off-Momentum detector. Future development will focus on further improving the timing jitter and scaling up to meet the requirements of the large-scale TOF system.

The calorimeter readout in ECCE will make use of a common digitizer design for all calorimeter systems. The development will start with the existing 64-channel, 14-bit ADCs running at six times the RHIC bunch crossing frequency of just below 10 MHz, at about 60 MHz designed for the sPHENIX calorimeters. ECCE will have a common digitizer design for all calorimeters, although the form factors may differ depending on the detector implementation. It is likely that the sampling frequency will be higher based on the detector requirements. The ECCE calorimeter subsystem includes a very high channel count, however no custom ASIC development is considered because the existing sPHENIX 64-channel 14-bit ADC design is proven and reduces the number of separate electronics designs that need to be developed, verified, and maintained throughout the lifetime of the experiment.

9. Computing plan

The ECCE consortium plans to deploy a federated computing model for the EIC, where multiple facilities are used. A similar strategy has been successfully deployed by the LHC in the form of the Worldwide LHC Computing Grid (WLCG) [42].

ECCE has developed a tiered "Butterfly" model for EIC computing as shown in Figure 28 [43]. In this model, both compute and storage resources are distributed with data storage focused at the Echelon 1 sites. This means access to data by users will be performed by connecting Echelon 3 sites directly to Echelon 1 sites. The Echelon 1 sites will themselves provide significant compute capability, but will also farm out large campaigns to Echelon 2 sites, taking advantage of the diverse computing resources available at collaborating institutions.

We have adopted a fixed-latency offline computing model where both the final calibration and reconstruction of raw data occur within 2-3 weeks of acquisition [43] with resource requirements shown in Table 9. During this period, raw data will be buffered on disk at all of the Echelon 1 sites, along with permanent archival copies on tapes. Final calibration will be performed semi-automatically including accumulating sufficient data for tracker alignment and energy scale calibration of the calorimeters. The ECCE computing team is also pioneering the application of state-of-the-art AI/ML algorithms in detector optimization [44, 24], simulation, and PID [45], as well as real-time reconstruction in streaming readout [46, 47], data reduction [48], and signal processing [49]. AI/ML will continue to play an integral and essential role in the ECCE online and offline computing. After calibration, data processing will be released to multiple sites including HTC facilities at both Echelon 1 and 2 sites as in Fig. 28. We expect that the produced simulation sample will focus on 10% of the EIC collision cross-section that is directly relevant for the signal and background of the core ECCE physics program. These events will be simulated to $O(10)$ times the statistics in real data to constrain systematic uncertainty from the simulated sample to be much smaller than the data statistical uncertainty. The projected simulation resources are equivalent to the needs shown in the data reconstruction as in Table 9.

During the development of this proposal, a detailed detector model was simulated and reconstructed taking advantage of years of ongoing development and validation with the Fun4All-EIC/sPHENIX software [25, 50]. Fun4All was determined to be the best software stack for the ECCE proposal studies, for expediency, reliability and its familiarity within the software team. Software is constantly evolving and choices will be re-evaluated in the coming months to ensure that over the next decade the ECCE software will incorporate the most advanced framework and packages with the aim of delivering a high performance, user-friendly, and reliable software stack. For example, the inclusion of AI as a tool to optimize detector design [44] has been utilized within the ECCE software stack as described in Ref. [24]. Another example includes the integration of A Common Tracking Software (ACTS) package [51] as highlighted in Ref. [52], and used in preliminary ECCE tracking pattern recognition and efficiency studies.

10. Infrastructure/Integration

The interaction region has an overall length of 9.5m. The ECCE detector extends from -4.5m to 5.0m around the origin. A total of half a meter of space between the end caps and the first interaction region magnets is reserved for vacuum pumps, valves, etc. The ECCE detector has an outer radius of 2.67 meters, which fits into the constraint given by the Rapid Cycling Synchrotron (RCS) located at 3.35m. To achieve the necessary alignment of the magnet with the electron direction the detector is rotated by 8 mrad in the horizontal plane.

The central detector features service gaps for routing out cables and services. For example, service gaps between the central barrel and the forward calorimeter assembly and the backward flux return are envisioned, as indicated in the Sketchup mechanical model on the cover page. Additional space between the inner detectors and hpDIRC, and barrel EMCal and cryostat allow for routing cables out towards the service gaps. The beam pipe diameter increases in radius from the interaction point to the end caps[1], and thus includes several sections divided by flanges. This has to be taken into account for detector installation and servicing. For example, the diameter of the beam pipe flange at the location of the EEMC determines the configuration of the first layer of $PbWO_4$. The beam pipe would need to be disassembled for the EEMC to be inserted/extracted from its nominal position. To maximize the EEMC acceptance and allowing for easy access the ECCE detector includes an option to separate out the inner EEMC. Taking into account the beam pipe diameter, the outer endcap detectors like the forward calorimeter assembly are foreseen to follow a clam shell design.

11. Technology Selection, Risk and R&D

While the ECCE detector design seeks to minimize risk through strategic re-use and the selection of mature, yet state-of-the-art detector technologies, there are nevertheless risks associated with some ECCE detector technology choices. Our strategy has been to clearly identify these risks and develop an appropriate mitigation strategy, either through developing alternatives should the risks be realized or eliminating risk through an aggressive R&D program. We have developed an extensive risk log for the ECCE proposal that includes risk impact, likelihood and mitigation strategy for a wide array of technical and cost & schedule risks.

A list of specific risks related to the ECCE technology selection includes:

- **BaBar Solenoid:** As a mitigation against the schedule risk posed by a potential problem with the BaBar solenoid developing during sPHENIX running, we plan to proceed with the initial engineering and design for a replacement magnet. This work will be carried out by CEA/Saclay in close collaboration with Jefferson Lab. A final decision to proceed with the BaBar solenoid or produce a new magnet will be taken in mid-2023 after the performance of the BaBar solenoid during the first year of sPHENIX running is reviewed by a panel of experts. The risk-mitigation decision tree is shown in Figure 29. Assuming a five-year construction for a new magnet, consistent with the duration

[1] this is necessary to allow the cone of proton/neutron and nuclear breakup particles to pass through

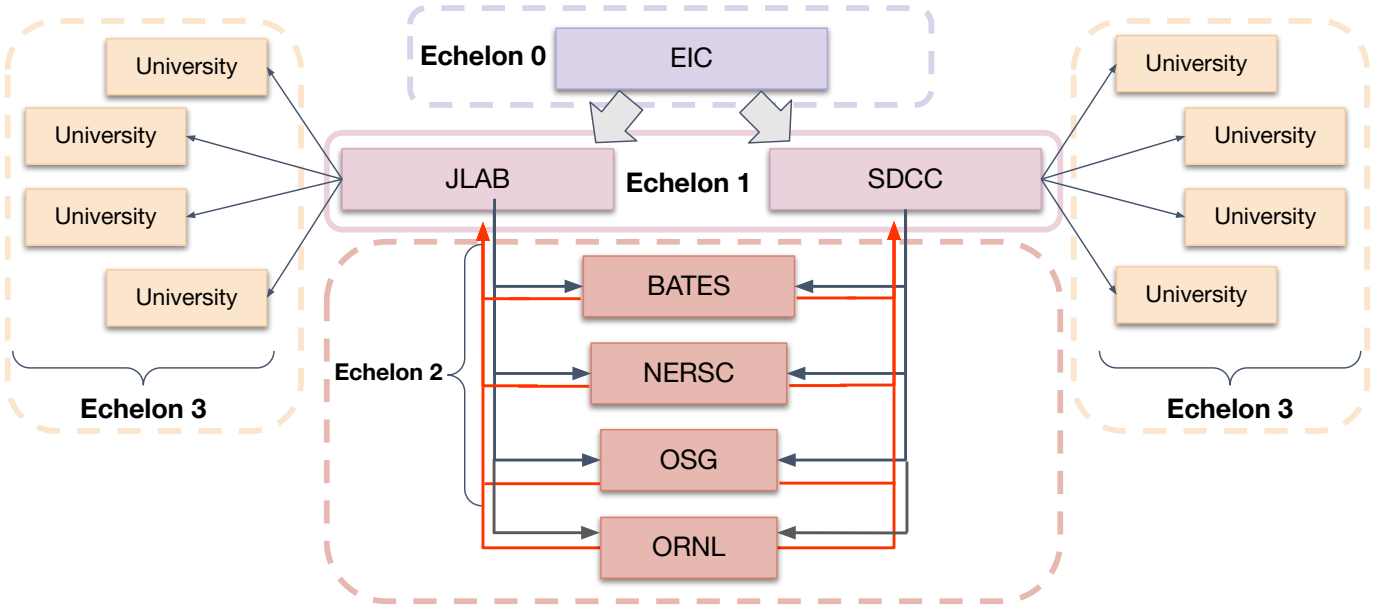

Figure 28: EIC Butterfly model of federated offsite computing [43]. In this model, nearly all storage is contained in echelon 1 while large portions of the raw data processing is delegated to multiple HTC/HPC facilities.

Table 9: Estimate of raw data storage and compute needs for first three years of ECCE, assuming ramp up to full luminosity by year 3 [43]

	ECCE Runs		
	year-1	year-2	year-3
Luminosity	10^{33}cm^{-2}s^{-1}	2×10^{33}cm^{-2}s^{-1}	10^{34}cm^{-2}s^{-1}
Weeks of Running	10	20	30
Operational efficiency	40%	50%	60%
Disk (temporary)	1.2 PB	3.0 PB	18.1 PB
Disk (permanent)	0.4 PB	2.4 PB	20.6 PB
Data Rate to Storage	6.7 Gbps	16.7 Gbps	100 Gbps
Raw Data Storage (no duplicates)	4 PB	20 PB	181 PB
Recon process time/core	5.4 s/ev	5.4 s/ev	5.4 s/ev
Streaming-unpacked event size	33kB	33kB	33kB
Number of events produced	121 billion	605 billion	5,443 billion
Recon Storage	0.4 PB	2 PB	18 PB
CPU-core hours (recon+calib)	191M core-hours	953M core-hours	8,573M core-hours
2020-cores needed to process in 30 weeks	38k	189k	1,701k

of new SC magnets recently built as part of the Jefferson Lab 12-GeV Upgrade project, the ECCE schedule for detector construction and assembly would remain consistent with an early CD-4A date if procurement of a replacement magnet is determined to be necessary.

- **SciGlass Calorimetry:** The use of SciGlass for electromagnetic calorimetry in the ECCE barrel offers a low-cost solution to large area electromagnetic calorimetry with excellent energy resolution. The performance of SciGlass has been demonstrated in short (20 cm) bars. The performance validation of longer blocks is part of the ongoing EIC project R&D (eRD105) and the demonstration of large scale commercial production with high quality and uniformity is part of an ongoing Phase2 SBIR/STTR. The ECCE strategy to address the risk associated with SciGlass, if it is realized, is two-fold: if SciGlass cannot be produced on-schedule in sufficient quantities for ECCE needs, one option would be to refurbish half of the

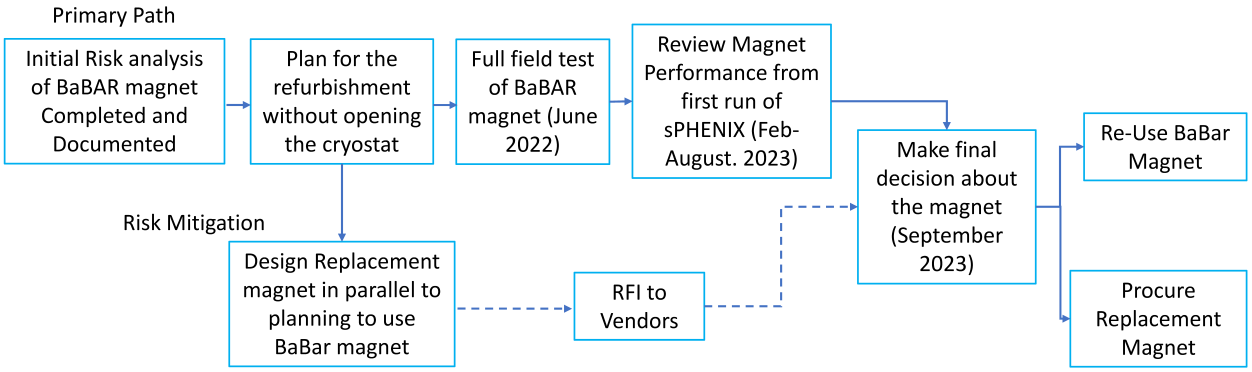

Figure 29: Decision tree for the risk mitigation strategy associated with the reuse of the BaBar solenoid.

existing sPHENIX W/SciFi calorimeter to cover half of the ECCE acceptance, reducing the overall need for SciGlass. The refurbished sPHENIX calorimeter could meet required energy resolution in the forward ($\eta > 0$) acceptance, albeit with lower performance compared with SciGlass. SciGlass would still be used at the backwards direction ($\eta < 0$) where optimal energy resolution is required. If SciGlass were unavailable in sufficient quantity for the backwards region as well, the remaining half of the ECCE acceptance could be covered with PbGl towers at additional expense.

- **Cylindrical μRWell Tracking:** The ECCE experiment utilizes μRWell tracking layers in the central barrel as a low-mass, cost-effective means to provide the additional tracking points required to achieve the required momentum resolution. While cylindrical μRWell detector should be technically possible, it remains to be demonstrated that they can provide stable operation at the required 55μm resolution in a magnetic field. ECCE plans an aggressive R&D program, working with our international partners, to demonstrate the performance of cylindrical μRWell detectors and address any technical challenges that may arise.

- **AC-LGADs:** ECCE plans AC-LGAD sensors for TOF not only in the forward and backwards region but in the central barrel as well. Cylindrical detectors based on LGAD sensors have not been previously demonstrated, and AC-LGAD sensors require additional R&D to demonstrate and characterize their performance and suitability for use in both the TOF and Roman Pot detectors in ECCE. To mitigate this risk, ECCE plans a comprehensive R&D for AC-LGAD sensor and readout development, characterization and readout to ensure the required timing resolution can be achieved.

- **B0 Detector:** The current design of the B0 detector calls for a crystal calorimeter to be installed after the tracking stations in the B0 warm bore to enable studies of physics processes that require γ energy measurement such as u-channel DVCS. The installation, integration and maintenance of this detector present severe mechanical challenges due to the tight constraints in the magnet bore that will require detailed mechanical designs. If it is determined that installation of a crystal calorimeter is not feasible we will be forced to accept the loss of scope and install only the tracking planes.

In addition to detailing risks in the ECCE risk registry, we also document potential risk opportunities. We list a few representative examples here, additional information is available in the ECCE risk registry and opportunity log, both of which are available in the ECCE supplemental material.

- **Reduction of the number of hpDIRC sensors:** R&D performed for the PANDA DIRC suggests that the sensor coverage can be reduced by up to 30% without significant impact on the PID performance. A positive outcome of the simulation study and validation in test beam would allow ECCE to take advantage of this opportunity.

- **Improved ITS3 sensor yields:** Si tracker costs could be reduced if ITS3 sensor yield is higher than anticipated. We intend to take advantage of knowledge gained from ALICE ITS3 production, as well as with the foundry to optimize sensor yields.

- **hpDIRC lightguide shape:** Currently three options are being considered for the lighguide section of the bar box, which couples the narrow radiator bars to the lenses and prism. Use of one wide plate per bar box would be the most cost efficient. We intend to perform a simulation study and a test experiment with particle beams to validate this potentially cost-saving and performance-enhancing hpDIRC option for ECCE.

12. Upgrades

The ECCE baseline detector can be augmented with additional upgrades that either enhance or expand the existing physics reach:

- **Dual-Readout Calorimetry:** The addition of a dual-readout calorimeter, replacing the FEMC and LFHCAL in

the forward region would provide a significant improvement in energy resolution for hadrons in the forward region. Because the tracking momentum resolution worsens with increasing momentum while the calorimeter energy resolution improves with increasing energy, the association of tracks with high-resolution clusters in the forward calorimeters can be used to improve the knowledge of high momentum tracks (the so-called "particle-flow" approach). With a dual-readout calorimeter, the crossover point between the tracking and calorimeter resolution would be pushed lower, enabling this improvement for a larger fraction of the tracks detected in the forward arm. Adding such improved capabilities to ECCE would improve measurements of SIDIS hadrons, TMD measurements with jets, and the ability to reconstruct event kinematics using the hadronic remnants. The Korean HEP community is very interested in deploying dual-readout calorimetry in ECCE as they develop the technology for future high-energy facilities.

- **Muon Chambers:** The addition of muon chambers to the ECCE baseline would enable the improved detection and tagging of semi-leptonic decays of heavy flavor. ECCE collaborators in Israel have expressed an interest in providing this upgrade as an in-kind contribution to ECCE. The ability to use muons for such processes as DVCS and DVMP removes an ambiguity between the produced leptons in the electron channel and the scattered electron. Such an upgrade can enhance the ability of ECCE to produce the science in the EIC white paper and NAS report.

- **Hadron Arm High-Rapidity Tracking Layer:** The addition of a small, high rapidity AC-LGAD layer ($3.0 < \eta < 3.5$) in front of the forward electromagnetic calorimeter could improve track momentum resolution for very high momentum ($p_T > 20$ GeV/c) charged tracks. It would also allow the detection of hadrons that enter the forward calorimeters from outside the acceptance of the inner tracker. This would be very beneficial for the deconvolution of overlapping clusters in the forward calorimeters as a necessary component to implementing a particle flow algorithm for the reconstruction of forward jets.

- **Backwards Hadronic Calorimeter:** While the ECCE baseline does not include a backwards hadronic calorimeter in the electron-going region, the addition of such a calorimeter could contribute to the reconstruction of event kinematics by the double-angle of Jacquet-Blondel methods at high-y, and contribute to electron identification in the backwards region. Such a calorimeter could be based on the STAR FCS Fe/Sc hadronic calorimeter, with partial re-use of the existing STAR additional modules and new modules constructed to complete the acceptance. We have studied this extensively within ECCE, and a hadronic calorimeter in the backwards region is not required to pursue the science program in the EIC white paper or NAS report and therefore does not justify the substantial expense required at this time. However, it is possible as the EIC program matures and the EIC luminosity increases we may revisit this with a simple upgrade.

13. Summary

In summary, the ECCE detector has been designed to address the full scope of the EIC physics program as presented in the EIC white paper [3] and the NAS report. ECCE can be built within the budget envelope set out by the EIC project while simultaneously managing cost and schedule risks. This detector proposal has been reviewed and has been selected to be the basis for the project detector for the future collider.

14. Acknowledgements

We thank the EIC Silicon Consortium for cost estimate methodologies concerning silicon tracking systems, technical discussions, and comments. We acknowledge the important prior work of projects eRD16, eRD18, and eRD25 concerning research and development of MAPS silicon tracking technologies.

We thank the EIC LGAD Consortium for technical discussions and acknowledge the prior work of project eRD112.

We acknowledge support from the Office of Nuclear Physics in the Office of Science in the Department of Energy, the National Science Foundation, and the Los Alamos National Laboratory Laboratory Directed Research and Development (LDRD) 20200022DR.

This research used resources of the Compute and Data Environment for Science (CADES) at the Oak Ridge National Laboratory, which is supported by the Office of Science of the U.S. Department of Energy under Contract No. DE-AC05-00OR22725. The work of AANL group are supported by the Science Committee of RA, in the frames of the research project # 21AG-1C028. And we gratefully acknowledge that support of Brookhaven National Lab and the Thomas Jefferson National Accelerator Facility which are operated under contracts DE-SC0012704 and DE-AC05-06OR23177 respectively.

References

[1] National Academies of Sciences, Engineering, and Medicine, An Assessment of U.S.-Based Electron-Ion Collider Science, The National Academies Press, Washington, DC, 2018. doi:10.17226/25171. URL https://www.nap.edu/catalog/25171/an-assessment-of-us-based-electron-ion-collider-science

[2] R. Abdul Khalek, et al., Science Requirements and Detector Concepts for the Electron-Ion Collider: EIC Yellow Report, Nucl. Phys. A 1026 (2022) 122447. arXiv:2103.05419, doi:10.1016/j.nuclphysa.2022.122447.

[3] A. Accardi, et al., Electron Ion Collider: The Next QCD Frontier: Understanding the glue that binds us all, Eur. Phys. J. A 52 (9) (2016) 268. arXiv:1212.1701, doi:10.1140/epja/i2016-16268-9.

[4] A. Adare, et al., An Upgrade Proposal from the PHENIX Collaboration (2015). arXiv:1501.06197.

[5] F. Bock, et al., Design and Simulated Performance of Calorimetry Systems for the ECCE Detector at the Electron Ion ColliderTo be published in Nucl. Instrum. Methods A (in this issue) (7 2022). arXiv:2207.09437.

[6] First Authors, et al., Design and Simulated Performance of Tracking Systems for the ECCE Detector at the Electron Ion Collider, to be published in Nucl. Instrum. Methods A (in this issue) (2022).

[7] First Authors, et al., Computing Plan for the ECCE Detector at the Electron Ion Collider, to be published in Nucl. Instrum. Methods A (in this issue) (2022).

[8] First Authors, et al., Deep Learning-based Lepton Identification for the ECCE Detector, to be published in Nucl. Instrum. Methods A (in this issue) (2022).

[9] First Authors, et al., AI-assisted Optimization of the ECCE Tracking System, to be published in Nucl. Instrum. Methods A (in this issue) (2022).

[10] First Authors, et al., eA Diffractive Production with the ECCE Detector at the Electron Ion Collider, to be published in Nucl. Instrum. Methods A (in this issue) (2022).

[11] First Authors, et al., Exclusive and Diffractive Processes and Tagging with the ECCE Detector at the Electron Ion Collider, to be published in Nucl. Instrum. Methods A (in this issue) (2022).

[12] First Authors, et al., SIDIS Double Spin Asymmetries with the ECCE Detector at the Electron Ion Collider, to be published in Nucl. Instrum. Methods A (in this issue) (2022).

[13] R. Fair, EIC Technical Note EICTJ-O-DE-PLT-TD-0017-R00 (2021).
URL https://jlabdoc.jlab.org/docushare/dsweb/Get/Document-250033/21-045.pdf

[14] Letter of Intent: A Forward Calorimeter (FoCal) in the ALICE experiment (6 2020).

[15] J. Anderson, K. Bauer, A. Borga, H. Boterenbrood, H. Chen, K. Chen, G. Drake, M. Dönszelmann, D. Francis, D. Guest, B. Gorini, M. Joos, F. Lanni, G. L. Miotto, L. Levinson, J. Narevicius, W. P. Vazquez, A. Roich, S. Ryu, F. Schreuder, J. Schumacher, W. Vandelli, J. Vermeulen, D. Whiteson, W. Wu, J. Zhang, FELIX: A PCIe based high-throughput approach for interfacing front-end and trigger electronics in the ATLAS upgrade framework, Journal of Instrumentation 11 (12) (2016) C12023–C12023. doi:10.1088/1748-0221/11/12/c12023.
URL https://doi.org/10.1088%2F1748-0221%2F11%2F12%2Fc12023

[16] ECCE Consortium, Notes on the use of the BaBar solenoid in ECCE, ecce-note-det-2021-01 (2021).
URL https://www.ecce-eic.org/ecce-internal-notes

[17] ECCE Consortium, ECCE Tracking, ecce-note-det-2021-03 (2021).
URL https://www.ecce-eic.org/ecce-internal-notes

[18] G. A. Rinella, et al., First demonstration of in-beam performance of bent Monolithic Active Pixel Sensors (5 2021). arXiv:2105.13000.

[19] D. Colella, ALICE ITS 3: the first truly cylindrical inner tracker (2021). arXiv:2111.09689.

[20] X. Li, M. Brooks, M. Durham, Y. Corrales Morales, A. Morreale, C. Prokop, E. Renner, W. Sondheim, Forward silicon vertex/tracking detector design and R&D for the future Electron-Ion Collider (11 2021). arXiv:2111.03182.

[21] J. Blank, K. Deb, pymoo: Multi-objective optimization in python, IEEE Access 8 (2020) 89497–89509.

[22] H. Ishibuchi, R. Imada, Y. Setoguchi, Y. Nojima, Performance comparison of NSGA-II and NSGA-III on various many-objective test problems, in: 2016 IEEE Congress on Evolutionary Computation (CEC), IEEE, 2016, pp. 3045–3052.

[23] M. Rocklin, Dask: Parallel computation with blocked algorithms and task scheduling, in: Proceedings of the 14th python in science conference, Vol. 130, Citeseer, 2015, p. 136.

[24] ECCE Consortium, AI-assisted design of the ECCE detector: the ECCE Tracker Example, ecce-note-comp-2021-03 (2021).
URL https://www.ecce-eic.org/ecce-internal-notes

[25] ECCE Consortium, Selected topics in ECCE software and simulation, ecce-note-comp-2021-02 (2021).
URL https://www.ecce-eic.org/ecce-internal-notes

[26] F. Willeke, Electron Ion Collider Conceptual Design Report 2021 (2 2021). doi:10.2172/1765663.
URL https://www.osti.gov/biblio/1765663

[27] ECCE Consortium, ECCE Particle Identification, ecce-note-det-2021-04 (2021).
URL https://www.ecce-eic.org/ecce-internal-notes

[28] G. Giacomini, W. Chen, G. D'Amen, A. Tricoli, Fabrication and performance of AC-coupled LGADs, JINST 14 (09) (2019) P09004. arXiv:1906.11542, doi:10.1088/1748-0221/14/09/p09004.

[29] First Authors, et al., Design of the ECCE Detector for the Electron Ion Collider, to be published in Nucl. Instrum. Methods A (in this issue) (2022).

[30] U. Buchner, J. P. Donker, B. Spaan, J. Spengler, G. Schweda, D. Wegener, W. Schmidt-Parzefall, PERFORMANCE OF A SCINTILLATING GLASS CALORIMETER FOR ELECTROMAGNETIC SHOWERS, Nucl. Instrum. Meth. A 272 (1988) 695. doi:10.1016/0168-9002(88)90750-4.

[31] P. Ioannou, et al., The Experiment 705 electromagnetic shower calorimeter, Nucl. Instrum. Meth. A 332 (1993) 57–77. doi:10.1016/0168-9002(93)90741-Y.

[32] C. A. Aidala, V. Bailey, S. Beckman, R. Belmont, C. Biggs, J. Blackburn, S. Boose, M. Chiu, M. Connors, E. Desmond, A. Franz, J. S. Haggerty, X. He, M. M. Higdon, J. Huang, K. Kauder, E. Kistenev, J. LaBounty, J. G. Lajoie, M. Lenz, W. Lenz, S. Li, V. R.Loggins, E. J. Mannel, T. Majoros, M. P. McCumber, J. L. Nagle, M. Phipps, C. Pinkenburg, S. Polizzo, C. Pontieri, M. L. Purschke, J. Putschke, M. Sarsour, T. Rinn, R. Ruggiero, A. Sen, A. M. Sickles, M. J. Skoby, J. Smiga, P. Sobel, P. W. Stankus, S. Stoll, A. Sukhanov, E. Thorsland, F. Toldo, R. S. Towell, B. Ujvari, S. Vazquez-Carson, C. L. Woody, Design and beam test results for the sPHENIX electromagnetic and hadronic calorimeter prototypes, IEEE Transactions on Nuclear Science 65 (12) (2018) 2901–2919. doi:10.1109/tns.2018.2879047.
URL https://doi.org/10.1109/tns.2018.2879047

[33] C. A. Aidala, et al., Design and Beam Test Results for the sPHENIX Electromagnetic and Hadronic Calorimeter Prototypes, IEEE Trans. Nucl. Sci. 65 (12) (2018) 2901–2919. arXiv:1704.01461, doi:10.1109/TNS.2018.2879047.

[34] T. Horn, et al., Scintillating crystals for the Neutral Particle Spectrometer in Hall C at JLab, Nucl. Instrum. Meth. A 956 (2020) 163375. arXiv:1911.11577, doi:10.1016/j.nima.2019.163375.

[35] T. Horn, A $PbWO_4$-based Neutral Particle Spectrometer in Hall C at 12 GeV JLab, J. Phys. Conf. Ser. 587 (1) (2015) 012048. doi:10.1088/1742-6596/587/1/012048.

[36] Expression of Interest for the Electron Endcap Electromagnetic Calorimeter, https://indico.bnl.gov/event/8552/contributions/43186/attachments/31241/49300/EIC.EoI-EEEmCal-10312020.docx (2020).

[37] J. Bettane, et al., EEEMCal mechanical design and integration, https://wiki.jlab.org/cuawiki/index.php/EEEMCDocuments (2020).

[38] T. Horn, et al., eRD1: EIC Detector R& D Progress Reports 2017-2021 (2021).

[39] W. Erni, et al., Technical Design Report for PANDA Electromagnetic Calorimeter (EMC) (10 2008). arXiv:0810.1216.

[40] F. Guber, I. Selyuzhenkov (Eds.), Technical Design Report for the CBM Projectile Spectator Detector (PSD), GSI, Darmstadt, 2015.
URL https://repository.gsi.de/record/109059

[41] ECCE Consortium, ECCE Electronics and Readout/DAQ, ecce-note-det-2021-05 (2021).
URL https://www.ecce-eic.org/ecce-internal-notes

[42] J. Shiers, The Worldwide LHC Computing Grid (worldwide LCG), Computer Physics Communications 177 (1) (2007) 219–223, proceedings of the Conference on Computational Physics 2006. doi:https://doi.org/10.1016/j.cpc.2007.02.021.
URL https://www.sciencedirect.com/science/article/pii/S001046550700077X

[43] ECCE Consortium, ECCE Computing Plan, ecce-note-comp-2021-01 (2021).
URL https://www.ecce-eic.org/ecce-internal-notes

[44] E. Cisbani, A. Del Dotto, C. Fanelli, Williams, et al., AI-optimized detector design for the future Electron-Ion Collider: the dual-radiator RICH case, Journal of Instrumentation 15 (05) (2020) P05009. doi:https://doi.org/10.1088/1748-0221/15/05/P05009.

[45] C. Fanelli, J. Pomponi, DeepRICH: learning deeply Cherenkov detectors, Machine Learning: Science and Technology 1 (1) (2020) 015010. doi:10.1088/2632-2153/ab845a.
URL http://dx.doi.org/10.1088/2632-2153/ab845a

[46] F. Ameli, M. Battaglieri, M. Bondí, A. Celentano, S. Boyarinov, N. Brei, T. Chiarusi, R. De Vita, C. Fanelli, V.-d. Gyurjyan, et al., Streaming Readout of the CLAS12 Forward Tagger Using TriDAS and JANA2, arXiv preprint arXiv:2104.11388 (2021).

[47] Intelligent experiments through real-time ai: Fast data processing and autonomous detector control for sphenix and future eic detectors, dOE-

FOA-0002490 (2021).

[48] Y. Huang, Y. Ren, S. Yoo, J. Huang, Efficient data compression for 3d sparse tpc via bicephalous convolutional autoencoder, in: IEEE 2021 International Conference on Machine Learning and Applications, IEEE ICMLA", 2021. arXiv:2111.05423.

[49] S. Miryala, et al., Waveform processing using neural network algorithms on the front-end electronics, in: 22nd International Workshop on Radiation Imaging Detectors, 2021.

[50] T. sPHENIX collaboration, sPHENIX software repository, https://github.com/sPHENIX-Collaboration (2015).

[51] X. Ai, et al., A Common Tracking Software Project (June 2021). arXiv:2106.13593.

[52] J. D. Osborn, A. D. Frawley, J. Huang, S. Lee, H. Pereira Da Costa, M. Peters, C. Pinkenburg, C. Roland, H. Yu, Implementation of ACTS into sPHENIX Track Reconstruction, Comput. Softw. Big Sci. 5 (1) (2021) 23. arXiv:2103.06703, doi:10.1007/s41781-021-00068-w.